The complement system drives local inflammatory tissue priming by metabolic reprogramming of articular fibroblasts

Jasna Friščić[1,2], Martin Böttcher[2,3], Christiane Reinwald[1,2], Heiko Bruns[2,3], Benjamin Wirth[1,2], Samantha-Josefine Popp[2,3], Kellie Irene Walker[4], Jochen Ackermann[1,2], Xi Chen[1,2], Jason Turner[5], Honglin Zhu[1,2], Lisa Seyler[6], Maximilien Euler[1,2], , Philipp Kirchner[12], René Krüger, Triin Major[5], Oliver Aust[1,2], Daniela Weidner[1,2], Anita Fischer[7,8], Fabian T Andes[1,2], Zeljka Stanojevic[9], Vladimir Trajkovic[10], Martin Herrmann[1,2], Adelheid Korb-Pap[11], Isabel Wank[13], Andreas Hess[13], Johnathan Winter[14], Viktor Wixler[15], Jörg Distler[1,2], Günter Steiner[7,8], Hans P Kiener[7], Benjamin Frey[16], Lasse Kling[17], Karim Raza[5], Silke Frey[1,2], Arnd Kleyer[1,2], Tobias Bäuerle[6], Timothy Hughes[14], Anika Grüneboom[1,2], Ulrike Steffen[1,2], Gerhard Krönke[1,2], Adam Croft[5], Andrew Filer[5], Jörg Köhl[18,19], Kerstin Klein[4], Christopher D Buckley[5,20], Georg Schett[1,2], Dimitrios Mougiakakos[2,3], and Markus H Hoffmann[1,2]*

[1] Department of Internal Medicine 3 - Rheumatology and Immunology, Friedrich-Alexander University Erlangen-Nuremberg (FAU) and Universitätsklinikum Erlangen, Erlangen, Germany.
[2] Deutsches Zentrum fuer Immuntherapie, Friedrich-Alexander University Erlangen-Nuremberg (FAU) and Universitätsklinikum Erlangen, Erlangen, Germany
[3] Department of Medicine 5 for Hematology and Oncology, Friedrich-Alexander-Universität Erlangen-Nürnberg
[4] Center of Experimental Rheumatology, Department of Rheumatology, University Hospital Zurich, Zurich, Switzerland.
[5] Institute for Inflammation and Ageing, University of Birmingham, NIHR Birmingham Biomedical Research Centre, University Hospitals Birmingham NHS Foundation Trust, Birmingham, United Kingdom
[6] Institute of Radiology, Friedrich-Alexander-University Erlangen-Nürnberg (FAU) and Universitäts-klinikum Erlangen, 91054, Erlangen, Germany
[7] Division of Rheumatology, Department of Medicine 3, Medical University of Vienna, 1090, Vienna, Austria
[8] Ludwig Boltzmann Institute for Arthritis and Rehabilitation, Vienna, Austria
[9]Institute of Biochemistry, School of Medicine, University of Belgrade, Belgrade, Serbia
[10]Institute of Microbiology and Immunology, School of Medicine, University of Belgrade, Serbia
[11] Institute of Musculoskeletal Medicine, University Hospital Muenster, Albert-Schweitzer-Campus 1, D3, 48149, Muenster
[12]Institute of Human Genetics, Universitätsklinikum Erlangen and Friedrich-Alexander University Erlangen-Nürnberg (FAU), Erlangen, Germany
[13]Institute of Experimental and Clinical Pharmacology and Toxicology, Friedrich-Alexander University Erlangen-Nürnberg (FAU)
[14]Division of Infection and Immunity, School of Medicine, Cardiff University, Cardiff, UK
[15]Institute of Molecular Virology (IMV), Centre for Molecular Biology of Inflammation (ZMBE), Westfaelische Wilhelms University Muenster, Muenster, Germany
[16] Department of Radiation Oncology, Friedrich-Alexander-Universität Erlangen-Nürnberg, Universitätsklinikum Erlangen, Erlangen, Germany
[17] Innovations-Institut für Nanotechnologie und korrelative Mikroskopie, Forchheim, Germany
[18] Institute for Systemic Inflammation Research, University of Lübeck, Lübeck, Germany
[19] Division of Immunobiology, Cincinnati Childrens Hospital Medical Center and University of Cincinnati College of Medicine, Cincinnati, OH, USA

[20] Kennedy Institute of Rheumatology, University of Oxford, Oxford, UK

*to whom correspondence should be addressed:
Markus Hoffmann, Universitätsstraße 25a, 91054 Erlangen, phone: +49-9131-8543024, fax: +49-9131-8535776, email: markus.hoffmann@uk-erlangen.de

Summary

Here, we define the molecular and cellular mechanism of inflammation-mediated tissue priming that determines recurrence of arthritis at specific predilection sites. Re-exposure of joints to inflammatory stimuli caused prolonged and aggravated clinical signs of experimental arthritis as well as higher levels of inflammation and tissue damage. Tissue priming developed locally and was independent of the adaptive immune system, but progressively spread to contralateral joints. Fibroblasts isolated from paws repeatedly exposed to inflammatory stimuli ("primed fibroblasts") exhibited enhanced metabolic activity and NLRP3 inflammasome activation leading to functional changes with higher migration, invasiveness and osteoclastogenic potential. Human fibroblasts derived from established arthritis exhibited a similar primed functional phenotype as compared to fibroblasts from very early arthritis or non-inflamed joints. Transcriptomic and epigenomic analyses revealed upregulation of the complement system and confirmed metabolic reprogramming in primed fibroblasts. Genetic and pharmacological targeting of members of a complement C3 – C3a receptor – mTOR/HIF1α – NLRP3 axis reversed the primed fibroblast phenotype, induced a pro-resolving senescet phenotype and abrogated inflammatory tissue priming *in vitro* and *in vivo.* Our results suggest that inflammatory tissue priming is a process that leads to intracellular complement C3/C3aR activation and mTOR/HIF-1α-mediated metabolic activation of fibroblasts that trigger enhanced NLRP3 inflammasome activity and in consequence facilitate recurrence of inflammation.

Introduction

Although inflammation is usually a self-limiting process, inflammation can recur under certain circumstances leading to chronic inflammatory disease (Schett and Neurath, 2018). Such recurrence (or flare) of inflammation mostly involves specific sites which have been previously affected and for some, yet to be identified, reason are more prone to be revisited by inflammation. The underlying mechanism for this "inflammatory tissue priming" is currently unknown. Nonetheless, it is a highly conserved process and a common phenomenon in different inflammatory diseases. For instance, the chronic inflammatory phase in rheumatoid arthritis (RA) is often preceded by a period where bouts of inflammation alternate with episodes of non-active disease (McInnes and Schett, 2011; Scott et al., 2010). This recurrent shift between active and silent periods is also well-known in gouty arthritis which typically involves spurious inflammatory attacks revisiting the same joint regions before the condition becomes a persistent and disabling arthropathy (Richette and Bardin, 2010). Furthermore, in juvenile arthritis, stable patterns of joint distribution of the disease associated with distinct outcomes have been described (Eng et al., 2019). Hence, understanding how inflammatory tissue priming controls the transition from acute self-limiting to chronic inflammation is of seminal importance in a variety of diseases.

Previous findings suggest that inflammatory tissue priming is closely related to the exposure of resident cells to danger signals. There is ample evidence that danger associated molecular patterns (DAMPs) activate innate effector immune cell populations in the target tissues which trigger cytokine release and inflammation. In gout, for example, tissue-resident phagocytes are activated by monosodium urate (MSU) crystals to produce interleukin (IL)-1 and attract neutrophils that mount inflammation (Martinon et al., 2006; Maueroder et al., 2015). Furthermore, repeated exposure of innate immune cells to danger signals leads to epigenetic and metabolic rewiring at the cellular level and enhanced responses to repeated stimuli. This so-called "trained immunity" has been shown to be antigen-independent and primarily serves the aim to more effectively defend against recurrent infections (Crowley et al., 2017; Dominguez-Andres et al., 2020; Heremans et al., 1990; Netea et al., 2011). However trained immunity can hardly explain the site-specific recurrence of inflammation.

Based on the finding that priming of cells by repeated inflammatory stimuli can be antigen-independent and considering clinical observations that flares preferentially occur at sites previously affected by inflammation, we hypothesized that priming of resident tissue may occur upon repeated exposure to danger signals. To test this concept, we have used a combination of experimental models of resolving and persistent inflammatory arthritis to delineate the mechanisms of inflammatory tissue priming. We show that repeated inflammatory insults induce functional changes in synovial fibroblasts *in vivo* that are associated with enhanced cellular metabolic turnover. These changes require activation of the complement system in fibroblasts, protect from inflammation-induced senescence, mediate inflammasome activation, and trigger a sustained inflammatory response accompanied by profound bone damage. We thus demonstrate that inflammatory tissue priming establishes local "stromal memory" that promotes site-specific recurrence of inflammation.

Results

Tissue priming and systemic inflammatory memory after repeated challenge with inflammatory stimuli

To study inflammation-induced tissue priming, we set up models in which rodents were repeatedly challenged by inflammatory stimuli either systemically or at local level, to investigate whether recurrent exposure leads to more pronounced and persistent inflammatory responses. Inflammation after repeated intraperitoneal injection of arthritogenic serum from K/BxN mice, a standard model for inflammatory arthritis (Christensen et al., 2016), was prolonged as compared to the inflammatory response after the first injection (Figure 1A). Similarly, re-induction of arthritis in doxycyline-inducible human tumor necrosis factor transgenic (iTNFtg) mice (Retser et al., 2013) resulted in an increased number of swollen digits and concomitant functional impairment of the paws (Figure 1B, Figure S1A). To more precisely assess the role of local tissue in this process, we sequentially injected inflammatory triggers directly into the hind paws (Figure 1C). After repeated injection of Wistar rat paws with zymosan, a yeast-derived DAMP recognized by Toll-like receptor 2 and dectin 1 (Song et al., 2015), prolonged arthritis developed in the same paw, indicating local inflammatory tissue priming, while injection into the previously non-injected ("naïve") contra-lateral paw did not lead to prolonged arthritis (Figure 1D). Very similar results demonstrating local inflammatory tissue priming were obtained in knees of BALB/c mice after intra-articular injection with zymosan (Figure S1B) and in mouse paws challenged with MSU crystals, as an alternative DAMP (Figure 1E). Injection of MSU crystals also primed the tissue for prolonged arthritis with zymosan (Fig. S1C). Clinical signs of prolonged arthritis in the re-exposed primed tissue were in accordance with enhanced inflammation, assessed by magnetic resonance imaging (MRI, Figure 1F and 1G) and histology of the paw and the knee, respectively (Figures S1D and S1E). Moreover, microcomputed tomography (µCT) revealed that local structural bone remodeling linked to arthritis (Czegley et al., 2018; Tuncel et al., 2016) was significantly enhanced in the repeatedly injected primed paw (Figure 1H, I, and S1F). Finally, inflammatory tissue priming was also reflected by hyperalgesic responses in the primed as compared to the non-primed paw (Figure S1G). These findings suggest a mechanism of local tissue sensitization that is conserved across different species, inflammatory triggers and different affection sites. This process causes sustained local inflammatory responses and delays the resolution of inflammation.

Interestingly, when the injection intervals were lengthened, enhanced and prolonged arthritis after reinjection of zymosan or MSU crystals was also observed in the contralateral paw that had been injected only once (Fig. 1J and S1H), suggesting the conversion from a tissue-specific priming to a systemic inflammatory memory. In agreement with this concept, MSU crystal-induced arthritis in the left paw resulted in an exacerbated swelling in the contralateral MSU-injected right paw 4 weeks after the first injection, and simultaneous mild edema in the left paw even when left uninjected (Figures 1K and 1L).

Synovial fibroblasts mediate inflammation-induced tissue priming

Prolonged paw swelling upon reinjection of zymosan or MSU crystals in the same paw immediately after resolution of arthritis was maintained in severe combined immunodeficient (SCID) and RAG1^{ko} mice (Figures 2A, 2B, S2A, and S2B), which are devoid of functional T- and B-cells (Bosma et al., 1989). Nonetheless, inflammation-induced tissue priming also occurred in antigen-induced arthritis, a T cell-dependent model of RA that relies on systemic immunization with methylated bovine serum albumin (mBSA) preceding local initiation of inflammation by intra-articular knee injection of mBSA (Brackertz

et al., 1977) (Figure S2C and S2D). In turn, the transfer of tissue priming to the contralateral paw that we observed upon prolonged time in between the injections was strongly suppressed in SCID mice (Figure S2E). Therefore, tissue priming can be induced by both innate and adaptive immune pathways that trigger inflammation. While local imprinting is independent of adaptive immunity, the primed state of the tissue is eventually transferred to other joints by mechanisms that depend on the adaptive immune system.

We hypothesized that in paws pre-exposed to an inflammatory attack, joint-resident cells might have undergone adaptation processes that prime subsequent local responses. Since synovial fibroblasts are known to be key players in the development and maintenance of arthritis (Bartok and Firestein, 2010), we cultured fibroblasts from mouse paws injected with MSU crystals once (-/MSU; non-primed synovial fibroblasts) or twice (MSU/MSU; primed synovial fibroblasts) and from non-injected (naïve) paws and transferred them into an MSU crystal-based arthritis model. After subsequent injection of MSU crystals *in vivo*, the -/MSU fibroblasts had seen the inflammatory trigger twice, while MSU/MSU fibroblasts had already been exposed 3 times to MSU crystals. Transfer of primed fibroblasts promoted a significantly prolonged course of arthritis already after a single injection of MSU crystals (Figure 2C), suggesting that fibroblasts can transfer inflammation-induced tissue priming. In contrast, the exacerbation of arthritis upon transfer of -/MSU fibroblasts was not statistically significant. This suggests that priming might be a stepwise, accumulating effect which is intensified with repeated stimulation.

MSU crystal- or zymosan-primed fibroblasts also more effectively promoted the differentiation of monocyte precursors into large, multinucleated tartrate resistant acid phosphatase $(TRAP)^+$ osteoclasts (Figure 2D and 2E) and showed more invasive properties in a matrix-associated transepithelial resistance invasion (MATRIN) assay (Wunrau et al., 2009) (Figure 2F), while cell proliferation *in vitro* was similar (Fig. S2F).

Together with synovial tissue macrophages, synovial fibroblasts constitute the major cellular components of the synovial membrane, which is the principal site of inflammation in arthritis. During arthritis, characteristic pathognomonic changes of the synovium occur, in which lining layer synovial tissue macrophages (STM) are dispersed (Culemann et al., 2019) and sublining fibroblasts expand (Croft et al., 2019). To investigate the impact of the interaction between synovial fibroblasts and STMs, we performed iterated MSU crystal-induced arthritis in mice that express a Cre recombinase under the Cx3cr1 promoter together with a Cre-inducible diphtheria toxin receptor (Cx3cr1cre:iDTR mice). Cx3cr1 is expressed by blood monocytes as well as by the pre- and perinatal precursors of all tissue-resident macrophages (Yona et al., 2013). To analyse the impact of STMs on tissue priming, we injected DT twice at day 5 and day 6 before the second injection of MSU crystals. At this time, STMs are specifically depleted in DT-treated Cx3cr1cre:iDTR mice, since blood monocytes repopulate within 48 hours after DT application (Culemann et al., 2019). The absence of STMs caused slightly enhanced general inflammation than in control mice, without having a specific effect on tissue priming (Figure 2G). These results are in accordance with the reported anti-inflammatory role of $Cx3cr1^+Trem2^+$ TRMs of the synovial tissue in murine and human arthritis (Alivernini et al., 2020; Culemann et al., 2019).

To investigate the effect that inflammatory tissue priming has on the formation of the synovial lining and sublining structures, we analyzed primed and non-primed as well as naïve fibroblasts in 3D synovial lining cultures (Figure 2H). In these organoids, synovial fibroblasts spontaneously form a synovial lining-like layer on the outside of a spheroid composed of synthetic extracellular matrix (ECM) (Kiener et al., 2010). Naïve fibroblasts established a single-layered structure reminiscent of the synovial lining in a healthy joint. In contrast, non-primed fibroblasts isolated from arthritic rat paws after the first

exposure to zymosan formed a thickened lining layer comparable to the hyperplastic synovial lining in inflammatory arthritis. Primed fibroblasts, however, lost their capacity to form a lining, but instead formed a densely interconnected cellular network within the ECM of the organ culture. Cells within this network formed threadlike connections to adjacent cells, resulting in higher numbers of interaction partners within the matrix. This aberrant behavior of primed fibroblasts could also be replicated by sustained co-incubation of naïve fibroblasts with zymosan during the formation of the 3D organoid (Figure 2H).

Spontaneous release of IL-6, a fibroblast-derived cytokine playing a key role in arthritis (Schett, 2018; Wolf et al., 2014), was elevated from both primed and non-primed fibroblast organoids as compared to naïve fibroblasts (Figure 2I, left panel), while IL-6 production upon re-exposure to zymosan *in vitro* was further increased in primed as compared to non-primed fibroblasts (Figure 2I, right panel). These findings indicate the development of an inherent inflammatory sensitization in fibroblasts, which is gradually established by repeated or sustained activation with an inflammatory stimulus.

Disintegration of the synovial lining layer in arthritis and increased accumulation of fibroblasts in the sublining and the infrapatellar fat pad was also found *in vivo* by three-dimensional light-sheet microscopy of primed mouse knees repeatedly exposed to zymosan (Figures 2J-M). Moreover, morphological changes and increased formation of cell-cell-connections were also observed by scanning electron microscopy in 2D cultures of primed fibroblasts (Figure S2H).

Transcriptomic analysis of fibroblasts during inflammation-induced tissue priming

To delineate the underlying mechanisms and consequences of fibroblast priming induced by repeated inflammatory stimuli, we performed bulk RNA-Sequencing on cultured naïve, non-primed (-/MSU) and primed (MSU/MSU) fibroblasts (Figures 3A-E). Gene set enrichment analysis (GSEA) identified several pathways being differentially active during the three fibroblast states, among them processes connected to inflammation (e.g., NF-κB, IL-6/JAK/STAT3 and the complement system) and canonical metabolic pathways (Figure 3A). Ingenuity pathway analysis (IPA) further confirmed metabolic changes (including glycolysis, glutaminolysis, and redox biology) and inflammatory activation with the complement system being specifically upregulated in primed fibroblasts (Figure 3B, Table S1). The integrin signaling canonical pathway was also increased in primed fibroblasts, which not only bears a connection to cellular invasiveness (Peters et al., 2012) but also impacts the function of complement components (Chen et al., 2012).

To confirm our findings, we repeated bulk RNA sequencing with a validation set of samples (n = 3) and a targeted mRNA enrichment protocol enabling an improved capturing of expression profiles. The results showed that non-primed and primed fibroblasts are distinct populations (Figure 3C) and confirmed upregulation of the complement system in primed fibroblasts, together with pathogenic fibroblast markers such as Thy1, fibroblast activation protein (FAP) and Cadherin 11 (Cambre et al., 2019; Chang et al., 2011; Croft et al., 2019; Kiener et al., 2009; Lee et al., 2007), inflammatory cytokines and chemokines, arthritis-associated DAMPs such as biglycan (*Bgn*) and *Tnc* (Cambre et al., 2019), and key metabolic pathways (Figures 3D-E, S3A-S3C, Table S2). Upregulation of complement components and IL-6 in primed fibroblasts was further confirmed by qPCR (Figure 3F). Furthermore, we observed upregulation of key mediators of osteoclast differentiation (e.g. *Tnfsf11*, *Csf1*, *Tnf*, *Il6*), and matrix metalloproteinases and other enzymes involved in bone destruction, such as *Adamts2* and *Mstn* in primed fibroblasts, while, with the exception of *Tnfrsf11b* (OPG) and *Il33*, negative regulators of osteoclast differentiation (such as Interferons, *Il3*, *Il4* or *Il10*) exhibited low or no expression. Although both *Tnfsf11* (RANKL) and *Tnfrsf11b* (OPG) were upregulated, the RANKL/OPG ratio was markedly

elevated in primed fibroblasts (Fig. 3G). Also molecules involved in enhanced bone remodeling in the context of arthritis (such as *Tgfb1* and bone morphogenetic proteins), and ECM components such as collagens (Figures 3E and S3A) exhibited enhanced expression in primed fibroblasts.

Evidence has arisen that reprogramming of innate immune cells and the aggressive phenotype of SF isolated from patients with RA (RASF) is mediated by epigenetic changes including modifications on DNA and histones (Araki et al., 2016; Ospelt et al., 2017; Ostuni et al., 2013). To integrate the expression changes in primed fibroblasts with chromatin accessibility we performed ATAC Seq analysis (Buenrostro et al., 2015) (Figures 3H-K, S3D). Interestingly, regarding genome wide chromatin accessibility, naïve and non-primed (-/MSU) fibroblasts formed a combined cluster, while primed (MSU/MSU) fibroblasts were markedly distinct (Figure 3H). Primed fibroblasts were characterized by increased chromatin accessibility at the transcription start sites (as defined by ATAC seq normalized taq counts) of many genes connected to inflammation, bone remodeling, and metabolism, among them *C3* and *Nlrp3* (Figures 3I - 3K). Genome-wide chromatin accessibility in primed fibroblasts paralleled their enhanced expression profile (Figure S3D).

To link our findings to specific subpopulations of cells, we next used single-cell RNA sequencing of FACS sorted $CD45^-$ cells from MSU crystal-injected paws (Figures 3L and 3M, Table S3). The results demonstrated that cells with high expression of complement components, such as *C3*, *C4b*, *Serpinf1*, *C1ra,* and *C1s1* were part of a fibroblast cluster showing enrichment of markers previously found to be upregulated in the sublining layer of the synovium (e.g.; *Clec3b*, *Gsn*, *Apod*, *Rarres2*, *Myoc*, and *Pi16*) that are connected to inflammation and vasculogenesis (Croft et al., 2019). Enumeration of cell subpopulation frequencies from bulk RNA-Sequencing by CIBERSORTx (Newman et al., 2019) revealed strong expansion of this sublining fibroblast (SL) subset in primed as compared to non-primed paws (Figure 3N). These transcriptomic data were corroborated by flow cytometric analysis, which showed that $Pdpn^+Thy1^+$ SL (Croft et al., 2019) were enriched in cultured fibroblasts from primed paws (Figure S3E). Also, flow cytometry analysis of collagenase-digested fresh paw tissue demonstrated that a population of $Pdpn^+Thy1^+$ SL fibroblasts with markedly increased expression of C3 was prominently enriched in primed paws already early after the second injection of MSU crystals, as compared to non-primed and naïve paws (Figures 3O - Q and S3F). Also the number of $CD45^+$ cells was significantly increased in primed paws at day 2 after the second injection of MSU crystals (Figure S3G).

Expression of complement in fibroblasts mediates functional changes and inflammatory tissue priming

Since the complement system was significantly upregulated in primed fibroblasts, we next examined its impact on inflammatory tissue priming. The three major routes of complement activation are the classical, alternative, and the lectin pathways, all of which converge on the central complement component C3. Downstream of C3 cleavage, the opsonin C3b propagates the complement cascade via C5, culminating in formation of the membrane attack complex and/or phagocytic uptake by scavenger cells, while the soluble anaphylatoxin C3a is an important modulator of the innate immune response (Coulthard and Woodruff, 2015; Irmscher et al., 2018; Liszewski et al., 2013; Markiewski et al., 2007; Ruan et al., 2010). Confocal microscopy confirmed strong upregulation of C3 protein in primed fibroblasts (Figure 4A). C3 was expressed in large amounts in the cytosol, was not confined to $Rab7^+$ late endosomes/lysosomes, but seemed particularly enriched in organelle structures reminiscent of the endoplasmatic reticulum (ER) or Golgi apparatus (Figure S4A). Extracellular stores of C3 could also be observed, suggesting that C3 may be secreted via the ER, similar to what was recently suggested to

occur in pancreatic β cells (King et al., 2019). To definitively assess the impact of complement on inflammatory tissue sensitization *in vivo* we performed the aforementioned local iterated MSU crystal-induced arthritis model in C3-deficient mice (Figure 4B). Interestingly, although C3 had been reported to influence leukocyte accumulation in response to MSU crystals into the peritoneum (Khameneh et al., 2017) the course of the first arthritis episode was not significantly different in the absence of C3. However, more persistent arthritis upon reinjection only occurred in wild-type (WT) but not C3-deficient mice ($C3^{ko}$), suggesting that inflammatory tissue priming *in vivo* depends on C3.

In contrast, treatment with the C5-blocking antibody BB5.1 (Zelek et al., 2020) failed to suppress tissue priming in BALB/c mice (Figure S4B) demonstrating that tissue priming is independent of terminal complement pathway activation. In support of this, NOD mice, which, among other inherent immune deficiencies such as functional deficits in NK cells, macrophages and dendritic cells (Kataoka et al., 1983; Pearson et al., 2003; Serreze et al., 1993) are homozygous for a deletion in the *Hc* gene that prevents complement C5 expression (Baxter and Cooke, 1993), exhibited inflammatory tissue priming upon challenge with MSU crystals (Figure S4C).

Complement is expressed in many different cell types of hematopoietic and non-hematopoietic origin (Lubbers et al., 2017). To assess the importance of C3 expression in non-hematopoietic cells we created bone marrow chimeras by transplanting WT bone marrow into $C3^{ko}$ lethally irradiated mice (Figure S4D). After transplantation of WT bone marrow, inflammatory tissue priming was still significantly reduced in $C3^{ko}$ recipient mice as compared to WT recipients (Figure 4C and 4D). These results suggest that inflammatory tissue memory is controlled by non-hematopoietic cells. To further determine the effect of C3 specifically expressed in fibroblasts on the development of inflammatory tissue priming, we transferred FACS sorted and cultured $CD45^{-}CD31^{-}$ fibroblasts derived from WT or $C3^{ko}$ mice, respectively, to previously non-injected paws of WT or $C3^{ko}$ recipient mice (Figure 4E). The comparison with the contralateral MSU crystal-injected paw enabled us to test if transfer of primed WT or $C3^{ko}$ fibroblasts induces inflammatory tissue priming. These transfer experiments confirmed that primed WT fibroblasts were able to imprint inflammatory tissue priming, while primed $C3^{ko}$ fibroblasts did not mediate this effect (Figure 4F and 4G). Interestingly, this ability of primed WT fibroblasts was also preserved to a certain degree in the paws of $C3^{ko}$ mice, suggesting that WT fibroblasts can imprint tissue priming independently of other C3-expressing cell types.

Fibroblasts from chronically inflamed joints exhibit functional changes such as increased proliferation, migration, and invasiveness (Bartok and Firestein, 2010). In line with these observations, primed fibroblasts isolated from MSU/MSU paws showed enhanced migration in a wound healing assay (Figures 4H and S4E) and exhibited a higher tissue-invasive potential (Figure 4I). Interestingly, both increased invasiveness and enhanced migration of primed fibroblasts were dependent on the expression of complement component C3 (Figures 4H, 4I, and S4E).

Metabolic changes in primed fibroblasts are dependent on the complement system and mediate transformation into pathogenic cellular functions

It is known that articular fibroblasts undergo metabolic adaptations during arthritis, including altered glucose and lipid metabolism as well as mitochondrial changes (Falconer et al., 2018). In fact, emerging evidence suggests that functional changes and metabolic plasticity are tightly interconnected (Folmes et al., 2012). Additionally, intracellular expression of complement components has recently been reported to be involved in metabolic reprogramming of T cells (Arbore et al., 2017; West et al., 2020). This phenomenon may also be relevant to other cell types with intracellular complement expression, such as fibroblasts (Liszewski et al., 2013).

To assess if functional changes of fibroblasts and inflammatory tissue priming are associated with metabolic rewiring and if such alterations are connected with the complement system, we analyzed the cellular metabolism of naïve, non-primed and primed fibroblasts. We observed increased activity of both glycolysis and respiration in primed (MSU/MSU) as compared to non-primed fibroblasts (Figures 5A-G). We detected enhanced glucose consumption and lactate secretion (Figure 5A), accompanied by elevated surface expression of the glucose transporter GLUT1 (Figure 5B). This observation is in line with the enhanced gene expression of key glycolytic enzymes such as *Hk2*, *Eno1*, *Ldha*, *Pdk1*, and *Pkm,* as assessed by RNA sequencing (Figure 5C). Metabolic flux analyses confirmed enhanced basal glycolytic activity particularly in primed and, to a lesser extent, in non-primed fibroblasts as compared to naïve fibroblasts (Figure 5D, left panel). Basal respiration showed a similar pattern (Figure 5D, right panel) indicating a general increase of metabolic activity in primed fibroblasts. Notably, metabolic flexibility of primed compared to non-primed fibroblasts was enhanced in terms of glycolysis (as indicated by increased glycolytic capacity and reserve, Figure 5E), but diminished in terms of mitochondrial respiration (as shown by elevated proton leak and reduced spare respiratory capacity, Figure 5F). Overall, the metabolic phenotype shifted towards aerobic glycolysis in primed fibroblasts (Figures 5G and 6A).

Blocking glycolysis *in vitro*, using a pharmacological inhibitor of the glycolytic pacemaker enzyme hexokinase 2 (HK2), 2-desoxy-D-glucose (2-DG), antagonized the increased migration (Figure 5H) and the enhanced invasiveness (Figure 5I) of primed fibroblasts. Moreover, the increased production of inflammatory cytokines such as TNFα, CXCL12, and IL-6 by primed fibroblasts upon re-stimulation *in vitro* was abrogated by 2-DG (Figure 5J). Treatment with 2-DG *in vivo* already diminished the first bout of MSU crystal-induced arthritis but also completely abrogated inflammatory tissue priming (Figure S5). These findings suggest that inflammatory tissue priming is closely related to enhanced glycolysis in primed fibroblasts.

While non-primed fibroblasts from WT and $C3^{ko}$ mice were bioenergetically very similar, the increase in metabolic activity seen in primed WT fibroblasts was completely absent in $C3^{ko}$ cells (Figure 6A), corroborating the complement system's role in driving the intrinsic metabolic adaptations of synovial fibroblasts during tissue priming. In fact, metabolic changes in synovial fibroblasts related to inflammatory tissue priming and the increase in GLUT1 expression in primed fibroblasts were not only abolished in the absence of C3, but reverted below the levels of non-primed and primed fibroblast (Figures 6B-D).

The downregulation of metabolic activity in $C3^{ko}$ fibroblasts indicated metabolic exhaustion or senescence. Indeed, aged cultured $C3^{ko}$ fibroblasts (passage 8) demonstrated increased accumulation of senescence-associated β-galactosidase (Figures 6E and S6A). In line with these results, the senescence markers *p15* (*Cdkn2b*), $p16^{INK4}$ (*Cdkn2a*) and *p21* (*Cdkn1a*) were upregulated in MSU/MSU fibroblasts from $C3^{ko}$ mice, while *Il6* expression was abolished (Figure 6F). Proliferation in unstimulatd WT and $C3^{ko}$ cells was not different, but was reduced in $C3^{ko}$ cells after two rounds of stimulation with TNFα *in vitro* (Figure S6B). This suggests that in the absence of C3, repeatedly stimulated fibroblasts adopt a senescent pro-resolving phenotype associated with resolution of inflammation (Montero-Melendez et al., 2020).

In human T cells, intracellular C3 is cleaved by Cathepsin L and the bioactive C3a subsequently engages the C3a receptor (C3aR) in lysosomes which results in tonic activation of mammalian target of rapamycin (mTOR) and sustained homeostatic levels of glycolysis required for cell survival (Kolev et al., 2015). Upon T cell stimulation C3 activation is increased and C3a and C3b are shuttled to the cell surface (West et al., 2020). Somewhat similarly, intracellular expression of C3aR was enhanced upon

priming and associated with an increased presence at the cell membrane (Figures 6G and S6C). These data from confocal microscopy were corroborated by transcriptomic and epigenetic analysis by bulk RNA-Seq and ATAC-Seq, respectively, which had shown overexpression of *Ctsl* and *C3ar1* mRNAs and increased openness in the TSS of these genes upon priming (Figures 3E, 3F and 3K).

To assess if C3aR has an effect on inflammatory tissue priming, we performed iterated MSU crystal-induced arthritis is $C3aR^{ko}$ mice (Humbles et al., 2000). Comparably to C3-deficient mice, inflammatory tissue priming upon repeated injection with MSU crystals was significantly reduced in $C3aR^{ko}$ mice (Figure 6H). The metabolic changes seen in cultured primed WT fibroblasts were not to be observed in cultured $C3aR^{ko}$ fibroblasts (Figures 6I, 6J, S6D and S6E). Rather the metabolic profile of primed $C3aR^{ko}$ fibroblasts was reminiscent of $C3^{ko}$ fibroblasts, with a marked shift towards a quiescent phenotype in cells from MSU/MSU paws. In line with this, primed $C3aR^{ko}$ cells had a significantly reduced capacity to transfer tissue priming to previously uninjected paws (Figures 6K and S6F). These data suggest that in mouse synovial fibroblast, C3aR is essential for C3-mediated metabolic reprogramming.

To investigate an involvement of mTOR in metabolic reprogramming of primed fibroblasts downstream of C3aR, we performed functional analysis of the mTOR pathway in $CD31^{-}CD45^{-}$ cells from collagenase-digested paws two days after the first/second injection of MSU crystals (Figure 6L). Phosphorylatof mTOR and of 4E-BP1 and S6 kinase, two translational regulators activated downstream of mTOR, were raised in primed fibroblasts. Additionally, we observed an increased expression HIF1α in primed WT but not C3-deficient fibroblasts (Figure 6M), a transcription factor that was shown to mediate glycolysis and survival in human synovial fibroblasts also under normoxic conditions (Del Rey et al., 2017). Phosphorylation of mTOR and HIF1α expression was also raised in cultured primed WT, but not $C3^{ko}$ or $C3aR^{ko}$ fibroblasts (Figure S6G). Inhibition of mTOR with rapamycin and treatment with KC7F2, a translational inhibitor of HIF-1α which also represses activation of 4E-BP1 (Narita et al., 2009) abrogated glycolysis of naïve fibroblasts upon repeated stimulation with TNF and increased senescence (Figures 6N and S6H). Respiration turned out to be completely absent in cells repeatedly stimulated with TNFα *in vitro* (Figure S6H).

Metabolic changes, including increased glycolysis, mitochondrial stress, and membrane electrolyte fluxes, have been shown to activate and/or modulate the activity of inflammasomes, particularly the NLRP3 inflammasome. Accordingly, a complement - metabolism - inflammasome axis has been proposed (Arbore and Kemper, 2016). Interestingly, *Nlrp3* was one of the highest upregulated genes in bulk sequencing data from primed fibroblasts (Figures 3D-F), which was confirmed by qPCR in WT but not in $C3^{ko}$ cells (Figure 6O). Furthermore, the activity of caspase 1 was enhanced in primed as compared to non-primed and naïve fibroblasts, as measured by the percentage of cells labeled by the fluorescent caspase-1 probe FAM-YVAD-FMK (FLICA) (Figure 6P). Accordingly, primed fibroblasts released more IL-1β into the cell culture supernatants (Figure 6Q). Interestingly, *in vitro* treatment with 2-DG diminished *Nlrp3* expression in both non-primed and primed fibroblasts (Figure 6R), suggesting that there is a direct connection between glycolysis and inflammasome expression in these cells. Finally, to test the effect of NLRP3 inhibition on inflammatory tissue priming, we used MCC950, a small molecule that specifically inhibits canonical and non-canonical activation of the NLRP3 inflammasome (Coll et al., 2015). Remarkably, MCC950 not only dampened MSU crystal-induced paw swelling, but also specifically abrogated inflammatory tissue priming and the associated bone damage (Figures 6S, S6I and S6J).

To assess if C3-associated metabolic reprogramming in fibroblasts also affects mechanisms of bone destruction, we first performed expression analysis of key mediators of osteoclast differentiation. The enhanced expression of *Tnfsf11*, *Tnf*, *Il1b* and *Il6* in primed fibroblasts was reduced to normal levels

upon treatment with 2-DG or in the absence of C3 (Figure S6K). *Csf1* (M-CSF) and *Tnfrsf11b* (OPG) expression was only diminished in $C3^{ko}$ mice. The RANKL-to-OPG ratio was consistently decreased upon 2-DG treatment and in $C3^{ko}$ fibroblasts, both on mRNA level and in supernatants (Figure S6L). Treatment with recombinant OPG, the Il-1 receptor antagonist anakinra and the TNFα decoy receptor etanercept strongly abolished osteoclast differentiation induced by primed fibroblasts (Figure S6M).
Taken together, these data indicate that inflammatory tissue priming is based on a bioenergetic switch of fibroblasts towards a more energetic phenotype, with a skewing towards aerobic glycolysis in response to C3/C3a/C3aR axis activation. This metabolic switch fundamentally changes the fibroblasts´ functional phenotype, increases the impact of recurrent inflammation, and mediates inflammatory bone destruction which is driven by TNF, IL-1 and disturbance of the balance between RANKL and OPG (Armaka et al., 2008).

C3 is expressed in a distinct population of human sublining synovial fibroblasts, implicated in arthritis.

To translate our observations in animal models to human disease, we assessed complement expression and metabolic switches in fibroblasts from the joints of RA patients. These cells (also known as "synovial fibroblasts") have been shown to synthesize several complement components, among them C3, C1r and C1s (Katz and Strunk, 1988; Neumann et al., 2002). We thus compared expression profiles of various complement components from publicly available single cell (sc) RNA analysis of human synovial tissue samples reported by the AMP (Accelerating Medicines Partnership Rheumatoid Arthritis and Lupus") consortium (Donlin et al., 2018; Zhang et al., 2019). We found *C3*, *C1r*, *C1s*, *CFB* and *Serping1* specifically upregulated in $CD45^{-}Pdpn^{+}$ fibroblasts derived from leukocyte-rich RA synovial tissue (Figure 7A), which is characterized by higher inflammation scores (Krenn et al., 2002; Zhang et al., 2019). In contrast, *C4a*, *C1qa* and *CD55* exhibited lower expression profiles in fibroblasts derived from patients with leukocyte-rich RA than with leukocyte-poor RA and/or osteoarthritis.
Transcriptomic analysis by scRNA sequencing (Figure 7B) and *in situ* hybridization using RNAScope (Figure 7C) showed that C3 expression is confined to distinct fibroblast subsets (scF1,2,3 and not scF4) and some macrophages (scM1,2) in the human joint. C3-expressing macrophages and fibroblasts were located in the sublining and absent from the lining layer. These findings are fully consistent with data from previous studies where C3 expression defined a particular subset of sublining inflammatory fibroblasts in mice and humans that also express CD34 (Croft et al., 2019; Donlin et al., 2018; Zhang et al., 2019).
Upregulation of complement component C3 in leukocyte-rich RA suggests that C3 expression is connected to local disease activity in the synovium. To assess if C3 expression is induced by inflammatory triggers in human articular fibroblasts we repeatedly stimulated cultured fibroblasts derived from the joints of RA patients with TNFα. C3 and C3a expression was upregulated gradually after repeated stimulation with TNFα both at the mRNA (C3) and protein level (C3/C3a) (Figures 7D and S7A).

To date, functional studies on fibroblasts have mostly been performed on cultured cells isolated from the joints of individuals with late stage, established RA. Little is known about the characteristics of fibroblasts during early stage arthritis or derived from healthy individuals. Therefore, the contribution of fibroblasts to the transition from early arthritis to established RA has remained relatively unexplored. To further translate our findings, we compared primary fibroblast samples from very early anti-citrullinated peptide antibody (ACPA)-positive RA (VERA; disease duration under 3 months) with samples from established rheumatoid arthritis (RA; disease duration between 6 and 36 months) and control subjects (NHD; patients with joint pain undergoing exploratory arthroscopy, in which the

synovium was found macro- and microscopically normal, with no inflammatory changes). All of these specimens were sampled from knee joints before initiation of treatment. We observed that fibroblasts from RA are characterized by increased invasiveness as compared to fibroblasts from VERA or controls (Figure 7E). Samples from RA but also from other chronic inflammatory forms of arthritis with active synovitis (gout and psoriatic arthritis) (Cimmino et al., 2011; Fromm et al., 2019) also exhibited accelerated wound healing in comparison to fibroblasts from VERA and NHDs (Figure 7F). Both invasiveness and migration in the wound healing assay showed trends to correlate with erythrocyte sedimentation rate (ESR) and C-reactive protein (CRP) serum levels (Figure S7B), establishing a connection between systemic inflammation and altered fibroblast function. Finally, we also observed a trend towards a glycolytic shift in fibroblasts from RA as compared to cells derived from VERA and NHD samples (Figure 7G) similar to the difference observed between primed and non-primed fibroblasts from murine arthritis models (Figure 5G).

Discussion

Herein, we describe inflammatory tissue priming, which mediates a more robust and prolonged response to repeated inflammatory triggers. This mechanism provides an explanation for disease relapses and for the transition from self-limited to chronic inflammation, which is a hallmark of many forms of inflammatory diseases. At the center of this process are fibroblasts, which undergo functional changes ("priming") after repeated exposure to inflammatory stimuli such as DAMPs. Mechanistically, complement activation in fibroblasts induces a metabolic activation with increased aerobic glycolysis and a shift to a pro-inflammatory state which involves pathogenic cellular function such as invasiveness, migration and NLRP3 inflammasome activation.

The resident tissue of inflamed joints is characterized by a tight network of synovial fibroblasts interacting with resident macrophages, endothelial cells and infiltrating myeloid cells, such as monocytes and granulocytes. Some myeloid cells can enter a transient state of non-responsiveness (tolerance) upon triggering with LPS or TNF and protect from inflammation (Culemann et al., 2019; Huber et al., 2017; Seeley and Ghosh, 2017). In contrast, fibroblasts gradually acquire a more disease-promoting phenotype and function during arthritis. For instance, upon stimulation with inflammatory triggers they mount an augmented production of proinflammatory mediators, such as IL-6 and CCL5, and a prolonged activation of nuclear factor (NF)-κB (Crowley et al., 2017; Klein et al., 2017; Nguyen et al., 2017). Such inflammatory changes in fibroblasts are accompanied by a proliferative and invasive cell behavior triggering tissue destruction (Bottini and Firestein, 2013; Buckley et al., 2001; Scott et al., 2010) and promoting leukocyte trafficking into joints (Buckley, 2017; Filer et al., 2017; Postigo et al., 1993). Modern cellular phenotyping of fibroblasts in the joints has uncovered that the $Thy1^{+}CD34^{+}$ subset of fibroblasts, which is found in the sublining regions of joints and closely interacts with vascular endothelial cells through NOTCH-3 signaling (Wei et al., 2020), is expanded in murine and human arthritis (Croft et al., 2019; Croft et al., 2016; Mizoguchi et al., 2018; Zhang et al., 2019). In our work, we show that this subset expresses high levels of complement factor C3 and other complement components and is the cellular basis for inflammatory tissue priming.

C3 is required for a metabolic rewiring towards a more energetic phenotype, which augments NLRP3 inflammasome activation in fibroblasts. Within the microenvironment of inflamed tissue, metabolic adaptation is a prerequisite for fibroblasts in order to maintain viability and functional competence. Emerging evidence therefore suggests that functional and metabolic plasticity are tightly interconnected (Falconer et al., 2018; Fearon et al., 2016; Folmes et al., 2012). Inflamed tissues

typically activate aerobic glycolysis in a "Warburg effect"-like manner. This is underlined by increased glucose metabolism in arthritis, visualized by positron emission tomography using fluoro-2-DG (Kubota et al., 2009). Pro-inflammatory mediators such as TNFα promote glycolytic flux (Garcia-Carbonell et al., 2016) and synovial fibroblasts in arthritis display an upregulation of glucose transporter 1 (GLUT1) expression and a metabolic shift towards glycolysis that correlates with pathogenic fibroblast function (Falconer et al., 2018; Gallagher et al., 2019; McGarry et al., 2017). In particular, hexokinase 2 mediates synovial lining hypertrophy, disease severity and tissue damage during arthritis (Bustamante et al., 2018; Garcia-Carbonell et al., 2016). These processes are reflected by a shift in the profile of energy metabolites in serum and urine of RA patients that correlates with both disease activity and the response to therapy (Falconer et al., 2018; Fearon et al., 2016; Tatar et al., 2016; Young et al., 2013). Furthermore, some of the established therapies in RA, such as methotrexate and leflunomide affect metabolism and function of fibroblasts in the joints (Lories et al., 2003; Vergne-Salle et al., 2005). Metabolic interventions targeting the altered metabolism in fibroblasts could therefore represent an interesting option for arthritis therapy, similar to the approaches tested in oncology (Tennant et al., 2010).

While in fibroblasts with functional C3 repeated inflammatory stimulation allowed metabolic activation, absence of C3 reverted this process and induced a quiescent fibroblast phenotype characterized by upregulation of senescence markers, that mediated resolution of inflammation and tissue protection. Little is known on the function of the complement system in resident tissue. However, recently Cambré and colleagues showed that upregulation of complement components in tendons and synovial tissue is associated with exacerbation of arthritis caused by increased mechanical strain (Cambre et al., 2018; Cambre et al., 2019).

Recent discoveries have unveiled previously unknown roles of the complement system in shaping inflammation via metabolic rewiring of cells and activation of inflammasomes. In particular, immune cells exhibit intracellular production of complement C3 and C5 that in turn activate cells in an autocrine manner (Arbore et al., 2016; Liszewski et al., 2013). Studies in T cells have shown that complement activation regulates the influx of amino acids and glucose and directly influences glycolysis (Kolev et al., 2015). In search for mechanisms underlying the impact of C3 on fibroblast activation, we assessed the role of the anaphylatoxin C3a that exerts its multiple pro- and anti-inflammatory effects through activation of its G-protein-coupled receptor on professional and non-professional immune cells and bone cells (Coulthard and Woodruff, 2015; Ignatius et al., 2011; Laumonnier et al., 2017). C3a is either generated canonically upon proteolytic cleavage from C3 by the C3 convertases of the alternative pathway or the classical/lectin pathways or non-canonically by several proteases from pathogens, the contact system or immune cells. For instance, human $CD4^+$ T cells generate C3a via cathepsin L-mediated cleavage, which mediates homeostatic survival of T cells and inflammatory cytokine production upon T cell stimulation by a mechanism involving shuttling to the plasma membrane (Liszewski et al., 2013). Such a "spring-loaded" system also seems to be at work in fibroblasts from the joint: C3 and C3aR were strongly overexpressed intracellularly in primed fibroblasts and C3aR increasingly colocalized with the plasma membrane upon fibroblast priming.

Mechanistically, this activation-induced metabolic reprogramming seems to critically involve activation of the mammalian target of rapamycin (mTOR) pathway, as determined by phosphorylation of mTOR and ist downstream regulators 4EBP1 and S6 kinase, and HIF-1α. An mTOR – HIF1α axis was previously also shown to be responsible for a switch to glycolysis in Th17 cells (Shi et al., 2011). HIF-1α is a transcription factor that causes sustained production of Il-1β downstream of glycolytic enzymes and metabolites (Tannahill et al., 2013). In RASF, HIF-1α promotes the expression of the inflammatory

cytokines IL-6, IL-8, TNF-α, and IL-1β, and various cell-cell contact mediators (e.g., IL-15 or VCAM-1), thus perpetuating the interaction between RASF and adaptive immune cells (Hu et al., 2016). HIF-1α is also a pro-survival signal that attenuates cytokine induced cell death in synovial fibroblasts and beta cells (Del Rey et al., 2017; Nomoto et al., 2020). In line with these findings, pharmacological inhibition of the mTOR pathway and of HIF-1α *in vitro* reduced priming-induced glycolysis and induced cellular senescence. This senescence phenoytpe, characterized by accumulation of SA-β-Gal and transcriptomic upregulation of senescence markers also occurred in C3-deficient fibroblasts after repeated stimulation *in vivo*. Given the pro-resolving phenotype of $C3^{ko}$ cells, the metabolic activation initiated by C3 seems to be a crucial premise for the override of the stimulation-induced shutdown that can be observed in primed fibroblasts.

Complement activation and metabolic changes can trigger a local pro-inflammatory environment by activation of inflammasomes (Asgari et al., 2013; Moon et al., 2015). Hence, both C3a and C5a induce NLRP3 inflammasome and IL-1β/IL-18 release from monocytes (An et al., 2014; Asgari et al., 2013; Carta et al., 2015; Cumpelik et al., 2016). In this context it is also interesting that NLRP3 inflammasome activation is driven in endothelial cells by enhanced glycolysis (Chen et al., 2013). Furthermore, glycolysis products promote LPS-induced NLRP3 activation in macrophages HIF 1α (Arbore and Kemper, 2016). Another route by which complement components regulate NLRP3 inflammasome activity is via increased generation of reactive oxygen species (ROS) (Arbore et al., 2016; Laudisi et al., 2013). Interestingly, in T cells from individuals with RA intracellular C3 activation is dysregulated and contributes to Th1 cell hyperactivity (Liszewski et al., 2013). Thus, a complement – metabolism – inflammasome axis drives recurrent inflammatory conditions, yet until our work, evidence that this network is operational in cells other than T cells has been missing.

Our human data strongly support the mechanistic concept that inflammatory tissue priming is based on a connection between local complement activation in fibroblasts, followed by metabolic changes and a shift towards a proinflammatory state in these cells. First, we showed that complement factor C3 activation is linked to a fibroblast subset that proliferates and orchestrates inflammation in arthritis (Croft et al., 2019; Croft et al., 2016; Mizoguchi et al., 2018; Zhang et al., 2019). Secondly, C3 expression is associated with a leukocyte-rich phenotype of arthritis, which is characterized by more severe inflammation suggesting inflammatory tissue priming (Zhang et al., 2019). Finally, synovial fibroblasts of patients with established but not early disease acquire a functional phenotype that strongly resembles the changes observed in the context of inflammatory tissue priming in arthritis models. Taken together these observations suggest that local functional changes of the resident tissue, which are orchestrated by complement activation and metabolic rewiring of fibroblasts, also mediate inflammatory tissue priming in humans. As such this mechanism has fundamental implications for human inflammatory disease. However, given the differences between the murine and the human complement systems, such as discrepancies in the expression of C3aR and CD46 complement regulatory protein (Neumann et al., 2002; Seya et al., 1998), the full details underlying intracellular C3 cleavage and receptor activation in human synovial fibroblasts need to be elaborated in further studies.

Proof of efficacy of complement-targeted therapy in human arthritis is still lacking (Holers and Banda, 2018; Trouw et al., 2017). The inhibitory anti-human C5 antibody eculizumab and the peptide C5aR inhibitor PMX-53 were both unsuccessful in clinical trials of RA (Vergunst et al., 2007). Of note, both act downstream of C3 cleavage in the complement cascade rather than targeting intracellular autocrine C3 function. Furthermore, our results indicate that complement factor C3/C3a-targeted

therapy is expected to prevent flares due to its effect on tissue priming rather than to decrease inflammation by directly interfering with effector cytokines or anaphylatoxins. Hence the design of studies using complement inhibition to control arthritis, i.e. to reverse inflammatory tissue priming, may need to be re-conceptualized.

While it is possible to effectively reduce inflammation in chronic inflammatory diseases such as arthritis or colitis with modern therapy, the cessation of treatment usually leads to the recurrence of the diseases, suggesting underlying mechanisms that are different from the effects of inflammatory effector cytokines (Schett et al., 2016). The data from our study suggest that such persistence of inflammation is based on inflammatory "memory" in the affected tissue. Our study also provides several levels of potential therapeutic interventions that could abrogate inflammatory tissue priming. These include the direct targeting of C3 (Mastellos et al., 2019), the reversal of metabolic rewiring by inhibitors of glycolysis (Akins et al., 2018), and small molecule inhibitors for the NLRP3 inflammasome (Yang et al., 2019). Notably such interventions may not lead to rapid suppression of acute inflammation, such as observed with anti-cytokine drugs, but they may reverse the underlying tissue priming, thus allowing physicians to successfully taper and even stop treatment with anti-inflammatory drugs without provoking disease flares.

Materials and Methods

Animals

Mice on the BALB/c and C57BL/6 backgrounds and Wistar rats were bred in house and kept in temperature- and humidity-controlled facilities at the University of Erlangen, Germany, the Medical University of Vienna, Austria, or the Faculty of Medicine, University of Belgrade, Serbia, respectively, with free access to food and water and 12 hours light/dark cycles. Complement C3-deficient $C3^{tm1Crr}$ mice were bought from Jackson, SCID mice (CB17/Icr-$Prkdc^{scid}$) and NOD/ShiLtJ mice were from Charles River Germany. $C3aR^{-/-}$ mice were from Jörg Köhl, University of Lübeck, Germany. $RAG1^{-/-}$ mice and $ColVI^{cre}$R26-tdTomato reporter mice, both on C57BL/6 background, were gifts from Prof. Mario Zaiss and Dr. Clemens Neufert, respectively, both from the University of Erlangen. Inducible hTNFtg mice (Retser et al., 2013)homozygous for the Tg_rtTA2S transgene and the human TNFα transgenes were kindly provided by Viktor Wixler (Westfaelische Wilhelms-Universität Muenster, Germany). Cx3cr1cre;iDTR mice were generated by breeding C57BL/6-Gt(ROSA)26Sortm1(HBEGF)Awai/J (iDTR) purchased from Jackson with STOCK Tg(Cx3cr1cre)MW126Gsat/Mmucd mice (Cx3cr1cre) (identification number 036395-UCD) from the Mutant Mouse Regional Resource Center (MMRC), a National Institutes of Health (NIH)- funded strain repository. Wistar rats were derived from Charles River. The animal studies were approved by the local ethical committees and conducted according to the guidelines of the Federation of European Laboratory Animal Science Associations (FELASA). All experiments were performed using age- and sex-matched littermate controls. If possible, mice were allocated randomly into groups by a computer-based random number generator (http://www.randomizer.org), so that each cage contained animals of every group to compensate for possible cage effects. Power analysis was performed before begin of the experiments on the basis of effect size estimates from previous experience.

Rodent inflammatory arthritis models

Monosodium urate (MSU) crystal induced monoarthritis was induced by injection of 1.4 mg MSU crystals suspended in 70 µl sterile PBS into the foot pads of the hind paws, between the metatarsals. MSU crystals were generated in house in a lipopolysaccharide (LPS)-free manner as described (Schauer

et al., 2014). Zymosan-induced monoarthritis was induced in mice similarly by injection of 300 µg zymosan (Sigma-Aldrich) suspended in 70 µl PBS. Rats received 1.7 mg zymosan suspended in 400 µl PBS. On day 0, MSU crystals/zymosan was injected only into the left paw while the right paw remained without injection. After resolution of the first arthritis episode (defined as reduction of paw thickness to <110% of values before injection, normally occurring between day 9 and 14), MSU crystals/zymosan was then injected into both paws. In some experiments complement factor C5 cleavage was blocked using the BB5.1 antibody ((Zelek et al., 2020), kindly provided by J. Winter, Cardiff university). To this end, 1 mg BB5.1 per mouse was delivered i.p. in 90 µl PBS twice a week, starting after the resolution of the first arthritis episode, 1 day before reinjection into both paws.

For analysis of the synovial lining by histology and light sheet microscopy 86 µg zymosan suspended in 20 µl PBS were injected intra-articularly into the knee as described (Culemann et al., 2019). Paw thickness during MSU crystal and zymosan-induced arthritis was monitored with an electronic caliper (Kroeplin) as described (Schauer et al., 2014) and areas under the arthritis curves (AUC) were calculated. Priming indices were defined as the ratio between the AUC of the second arthritis episode as compared to the AUC of the simultaneously occurring arthritis episode in the contralateral paw. K/BxN serum transfer arthritis (STA) was induced in BALB/c mice by intraperitoneal injection of 100 µl serum from arthritic K/BxN mice (kept in house at the University of Erlangen). After resolution of the first inflammatory bout, mice received another injection of serum. Arthritis was scored by measuring paw edema by caliper and additionally by a visual scoring system by assessing the level of swelling and redness in each paw, including the tarsus or carpus joints, as described (Kienhofer et al., 2014). The following scoring system was used: 0, no erythema/swelling; 1, erythema and swelling in up to two joints; 2, erythema and swelling in more than two joints or slight swelling of the ankle; 3, marked swelling of the ankle; 4, substantial swelling of the whole paw including toes/fingers. Antigen-induced arthritis (AIA) was elicited in C57BL/6 WT mice by two subcutaneous immunizations with 200 µg sterile-filtered methylated bovine serum albumin (mBSA) emulsified in 100 µl Complete Freund´s adjuvant (CFA) containing 1 mg/ml *M.tuberculosis,* followed by intra-articular injection of 100 µg mBSA suspended in 25 µl into the knee joint.

To induce hTNFα expression in iTNFtg mice 1mg/ml doxycycline (Sigma) and 5% sucrose was added to the drinking water for the time periods indicated in the figures. Doxycycline-containing water was protected from light and changed twice a week during the course of the experiments. For scoring of arthritis, the number of swollen digits was determined. The grip strength was assessed by placing the mice on the cage grid and using a scoring system ranging from 0 to -4: (0 = normal grip strength, -1 = mildly reduced, -2 = moderately reduced, -3 = severely reduced, -4 = no grip strength).

Multimodal imaging and analysis of features of murine arthritis models

For histomorphological analysis, paws or knees from naïve mice or after one or two injections of MSU crystals/zymosan were fixed overnight in 4% formalin, decalcified with EDTA, and embedded in paraffin. Paraffin sections were stained with haematoxylin & eosin or tartrate-resistant acid phosphatase for assessment of inflammation and osteoclasts, respectively. Analyses were performed on a Nikon microscope equipped with a digital quantification system (OsteoMeasure). Additionally, inflammation and bone remodeling were assessed *in vivo* as described (Czegley et al., 2018) at the Preclinical Imaging Platform Erlangen (PIPE) by a combination of ultra high field MRI (ClinScan, Bruker, Ettlingen, Germany) and CT using a preclinical scanner (Inveon, Siemens, Erlangen, Germany).

Additional microcomputed tomography (µCT) of the metatarsal and tarsal areas of mice during iterated arthritis was performed using the cone-beam Desktop Micro Computer Tomograph “µCT 40” by SCANCO Medical AG, Bruettisellen, Switzerland. The settings were optimized for calcified tissue

visualization at 55 kVp, 145 µA, and 200 ms integration time. For the segmentation of 3D-volumes, an isotropic voxel size of 8,6 µm was chosen. Using SCANCO´s operating system "Open VMS" osteophyte volumes were manually defined as volume of interest (VOI) along the bones. Then greyscale thresholds were set to include all voxels related to bone tissue for the measurement of bone volume.

Human subjects

Synovial tissue samples were collected from treatment-naïve patients in the Birmingham BEACON cohort with a new onset of clinically apparent arthritis and a symptom duration of less than 12 weeks, who at follow up fulfilled RA criteria (VeRA), from subjects with established, treated RA or from subjects undergoing exploratory arthroscopy for unexplained joint pain with no macro- or microscopic evidence of inflammation (NHD) (Filer et al., 2017). Further synovial tissue specimens were obtained from patients fulfilling the criteria for the classification of RA (Arnett et al., 1988) during joint replacement surgery at the Department of Orthopedic Surgery, Schulthess Clinic Zurich, Switzerland. Additional resident mesenchymal cell samples from individuals with RA, psoriatic arthritis, and gout were grown as described (Stebulis et al., 2005) from joint aspirates obtained for clinical reasons at the University clinics of Erlangen. All participants gave written informed consent as approved by the local ethic committees (new onset arthritis patients: West Midlands Black Country REC ref 07/H1203/57; Arthroscopy patients: West Midlands Black Country REC ref 07/H1204/191; Punctures No. 334_18B; No. 98_18B). Fibroblasts were cultured as described elsewhere (Ospelt et al., 2008) and used between passages 4 to 8 for all experiments. Patient characteristics of samples used are summarized in Table S4.
Leukocyte-rich and leukocyte poor RA in samples from the AMP cohort was defined as described (Zhang et al., 2019) by the Mahalanobis distance from osteoarthritis (De Maesschalck et al., 2000). Whereas leukocyte-rich RA tissues had higher Krenn synovitis scores and substantial infiltration of synovial T cells and B cells, leukocyte-poor RA tissues had cellular compositions more similar to those of OA samples. Synovial monocyte abundances were similar between leukocyte-rich, leukocyte-poor RA and OA samples (Zhang et al., 2019).

Isolation and culturing of fibroblasts from rodent paws.
Fibroblasts were isolated from the paws of mice or rats during different stages of K/BxN serum transfer arthritis, MSU crystal-induced arthritis, zymosan-induced arthritis, and from non-injected naïve paws. fibroblast cell suspensions of murine paws were prepared by gently rocking dissected and skin-flayed paws for 1 hour at 37°C in DMEM containing 2 mg/ml collagenase type IV (Worthington Biochemicals, LS004188). Cells derived from 2 to 3 paws were pooled and cells were then grown in DMEM (Gibco) supplemented with 10% heat-inactivated calf serum, (glucose (4.5 g/L), L-glutamine 2 mM), penicillin and streptomycin (1% each) antibiotics, and 1% fungizone (Amphotericin B, Sigma Aldrich). Medium was changed twice a week. After 3-4 passages fibroblasts are the dominant cell type, resulting in a homogenous cell population (Rosengren et al., 2007). Cells between passages 4 and 8 were used for the experiments and contained less than 2% $CD45^+$ or $CD31^+$ cells (Figure S2G), as determined by flow cytometry with a PerCP Cy5.5 conjugated anti-CD45 antibody (Biolegend 103132) and an AF647-conjugated anti-CD31 antibody (Biolegend, 102516).

RNA Sequencing and qPCR (transcriptomic analysis)
Isolation of RNA from mouse fibroblasts was performed using RNeasy kit (Qiagen 74104). One microgram of total RNA was reverse transcribed and real-time quantitative PCR was performed on a

Bio-Rad CFX96 Touch Real-Time PCR Detection System using qPCR Master Mix Plus for SYBR Green (Eurogentec RT-SN2X-03). Normalized gene expression values were calculated as the ratio of expression of mRNA of interest to the expression of reference gene (*β-actin* or *RPLP0*). Primer sequences were as follows:

Gene	Forward (5´- 3´)	Reverse (5´- 3´)
β-Actin (mouse)	TGTCCACCTTCCAGCAGATGT	AGCTCAGTAACAGTCCGCCTAGA
Csf1 (mouse)	AACGAGTCAGCAACTCAGCCA	TCCCTGGTACTTCTCTTGCCCT
Il1b (mouse)	AACCTGCTGGTGTGTGACGTTC	CAGCACGAGGCTTTTTTGTTGT
Il6 (mouse)	TGTGCAATGGCAATTCTGAT	TCCAGTTTGGTAGCATCCATC
Il6 (mouse)	CCGGAGAGGAGACTTCACAG	GGAAATTGGGGTAGGAAGGA
C3 (mouse)	GACGCCACTATGTCCATCCT	CCAGCAGTTCCAGGTCCTTTG
C4b (mouse)	GGAGCTAAAGATCCTTCGTACCTA	GCATCCCATGCGTATTCCAC
Nlrp3 (mouse)	TGCTCTTCACTGCTATCAAGCCCT	ACAAGCCTTTGCTCCAGACCCTAT
P15 (mouse)	AGATCCCAACGCCCTGAAC	CCCATCATCATGACCTGGATT
P16^{INK4} (mouse)	CCCAACGCCCCGAACT	GCAGAAGAGCTGCTACGTGAA
P21 (mouse)	GCAGATCCACAGCGATATCCA	AACAGGTCGGACATCACCAG
Tnf (mouse)	CAGGCGGTGCCTATGTCTC	CGATCACCCCGAAGTTCAGTAG
Tnfsf11 (mouse)	TGTACTTTCGAGCGCAGATG	AGGCTTGTTTCATCCTCCTG
Tnfrsf11b (mouse)	AGGAAGGGCGTTACCTGGA	GACAGCTCCGGTGCTTCAAG
RPLP0 (human)	GCGTCCTCGTGGAAGTGACATCG	TCAGGGATTGCCACGCAGGG
C3 (human)	CGGATCTTCACCGTCAACCA	GATGCCTTCCGGGTTCTCAA

For bulk RNA Sequencing of cultured fibroblasts sequencing libraries were prepared using either the TruSeq stranded total RNA kit with Ribo-Zero Globin (Illumina, 20020612) from 0.5 µg RNA or the TruSeq stranded mRNA kit (Illumina, 20020594) from 1 µg RNA. Libraries were subjected to single-end sequencing (101 bp) on a HiSeq-2500 platform (Illumina). The obtained reads were demultiplexed and converted to FASTQ format using bcl2fastq v2.17.1.14. Quality filtering was performed using cutadapt v. 1.18; total RNA libraries were alternatively filtered against a library of rRNA, tRNA, mt-rRNA and mt-tRNA sequences. Filtered reads were mapped to the mouse reference genome (Ensembl GRCm38) using the splice-aware aligner STAR (total RNA: STAR v 2.4.0i; mRNA: STAR v 2.6.1c). Read counts per gene were obtained by summing up reads for non-overlapping exons using Ensembl gene models (total RNA: HTSeq count, Ensembl annotation v84; mRNA: Subread v1.6.1, Ensembl annotation v96). The subsequent analyses were performed using the R package DESeq2 (Love et al., 2014) (total RNA: R v3.2, DESeq2 v1.10.1; mRNA: R v3.6.1, DESeq2 v 1.24.0).

For single cell RNA-Seq sorted CD45- non-hematopoietic cells of hind paws of mice at steady state and after a single or repeated injection of MSU crystals were subjected to 10x Chromium Single Cell 3' Solution v3 library preparation according to the manufacturer's instructions. Library sequencing was performed on an Illumina HiSeq 2500 sequencer to a depth of 200 million reads each. Reads were converted to FASTQ format using mkfastq from Cell Ranger 3.0.1 (10x Genomics). Reads were then aligned to the mouse reference genome (mm10, Ensembl annotation release 93). Alignment was performed using the count command from Cell Ranger 3.0.1 (10x Genomics). Primary analysis, quality control filtering (gene count per cell, unique molecular identifier count per cell, percentage of mitochondrial transcripts), clustering, identification of cluster markers and visualization of gene expression were performed using the Seurat (v3.1.1) package under R v3.6.1 (Butler et al., 2018). To be able to compare gene expression between conditions, data sets were integrated using the shared

nearest neighbor approach as implemented in Seurat v3.1.1. Prior to integration, cell counts were equalized by random downsampling of the larger sample.
Cell type abundance was enumerated from bulk RNA Sequencing by CIBERSORTx (Newman et al., 2019), using single-cell reference profiles. First, we used single cell RNA-Seq data to generate a gene signature matrix for each cluster. Then, we utilized S-mode batch correction and 1000 permutations with quantile normalization disabled for analyzing cell type relative fractions.

Assay for Transposase-Accessible Chromatin using sequencing (ATAC Seq)

C3 expression analysis in human rheumatoid arthritis-derived fibroblasts after stimulation with TNF
For double stimulation of fibroblasts with TNFα, we followed a protocol previously published by *Crowley* et *al.* (Crowley et al., 2017). 24h after seeding, fibroblasts were stimulated with the first dose of TNFα (10 ng/ml) for 24h. Afterwards, cells were washed twice with PBS, left untreated for 24h, followed by a second stimulation with TNFα (10 ng/ml) for another 24h. Cells were lysed for RNA isolation (Quick-RNA Micro Prep Kit, Zymo Research) or Western blotting after a total treatment period of 72h. For qPCR, total RNA was reverse transcribed, followed by real-time PCR (7900HT real-time PCR system, Life Technologies) using self-designed primers (Microsynth) and SYBR green (Roche). Dissociation curves and samples containing the untranscribed RNA were measured in parallel. Constitutively expressed human ribosomal protein large P0 (RPLP0) was measured for internal standard sample normalization and relative mRNA expression levels were calculated by the comparative threshold cycle method (ΔΔCt). For Western blotting, fibroblasts were lysed in Laemmli buffer (BioRad). Lysates were separated on 10% SDS polyacrylamide gels and electro blotted onto nitrocellulose membranes (Whatman). Membranes were blocked for 1h in 5 % (w/v) non-fat milk in TBS-T (20 mM Tris base, 137 mM sodium chloride, 0.1 % Tween 20, pH 7.6) and probed with antibodies against the C3 alpha chain (EPR2988; abcam), or α-tubulin (abcam) as endogenous control. As secondary antibodies, horseradish peroxidase-conjugated goat anti-rabbit or goat anti-mouse antibodies (Jackson ImmunoResearch) were used. Signals were detected using the ECL Western blotting detection reagents (GE Healthcare) and the Alpha Imager Software system (Alpha Innotech). Expression analysis of specific proteins was performed by pixel quantification of the electronic image.

Functional testing of synovial fibroblasts

Analysis of the barrier function properties and migratory capacity of fibroblasts. A Matrix-associated transepithelial resistance invasion (MATRIN-) assay was utilized as described (Wunrau et al., 2009) for testing the fibroblasts' invasive potential into extracellular matrix. A polycarbonate membrane of a filter mounted in a 6-well-dish was coated with a collagen matrix on one side, while MDCK-C7 epithelial cells (kindly provided by Prof. Thomas Pap, University of Münster, Germany) were seeded onto the other side. Following full establishment of the MDCK-C7 monolayer, fibroblasts were seeded onto the collagen matrices. Disturbing MDCK-C7 cell monolayer integrity by invading fibroblasts leads to a decrease of the transepithelial electrical resistance (TEER) that is measured with a set of electrodes connected to an ohm-meter. The electrical resistance was measured twice a day over the course of an experiment. All measurements were performed in triplicates and were terminated after total breakdown of the electrical resistance.

Wound healing and migration assay. For analysis of synovial fibroblast migration and proliferation we used a wound-healing assay with culture inserts (ibidi, 80209) in 6-well culture dishes. 20,000 fibroblasts were adjusted in 70 µl culture medium per chamber of an insert. After 24h, the inserts were

removed gently and the well was filled with 2 ml culture medium. The change in cell-covered area over time was monitored on a microscope equipped with a temperature and CO_2 control chamber (Keyence) and quantified using Photoshop CS6 software (Adobe).

3D organoids. The formation of an organized synovial lining was analysed in 3D synovial organ cultures (micromasses) as previously described (Kiener et al., 2010). Fibroblasts were resuspended in Matrigel Matrix (BD Biosciences) at a density of $1x10^6$ cells/ml. The obtained Matrigel Matrix cell suspension was plated in 1 ml/well Poly-2-hydroxyethylmethaacrylate (poly-HEMA, Sigma-Aldrich) coated cell culture plates. After 35-50 min incubation at 37°C, Micromass-Medium (V = 2 ml) was added. fibroblasts were maintained in culture in DMEM/F12 (Gibco) supplemented with 10% FCS, 0.1 mM ascorbic acid, ITS supplement (BioWhittaker) and 1% penicillin-streptomycin at 5% CO^2, 37°C for 3 weeks until the organ culture had built a sphere. In some cultures, 50 µg/ml zymosan (Sigma) was additionally added. For analysis of 3D organ cultures, paraffin-embedded sections were stained with hematoxylin & eosin.

Measurement of interleukin 6 in rat articular fibroblasts. Levels of rat IL-6 in supernatants from 3D micromass cultures were determined by ELISA (OptEIA, BD Biosciences Pharmingen, San Diego, CA, US) according to the manufacturer´s instructions.

Analysis of senescence. For detection of senescence associated β-galactosidase (SA-β-Gal), aged fibroblasts from passage 8 were stimulated with 10 ng/ml TNFα on flat bottom 12-well plates for 24h. After washing with PBS, cells were left untreated for 24h, followed by a second stimulation with TNFα (10 ng/ml) for another 24h. Control cells were incubated without any stimulation with TNFα. SA-beta-Gal activity was then determined with a senescence detection kit (Abcam).

Metabolic mapping of fibroblasts

Glucose consumption and lactate secretion. Supernatants from cultured fibroblasts were harvested and made cell-free by centrifugation after 48h of culture. Concentrations of glucose and lactate were determined using a $SuperGL_{Compact}$ (Hitado, Möhnesee, Germany).

Flow cytometry. Fibroblasts were cultured for 48 h under standard conditions and harvested using Accutase (Thermo Fisher Scientific, Waltham, MA). Cells were manually counted by Trypan blue staining and used at $1x10^5$ cells per sample. Samples were washed once in FACS buffer (PBS/0,5%BSA, 0,01%NaN_3, 0,5 mM EDTA) and incubated for 30 min at room temperature with FcR blocking reagent (Miltenyi Biotec, Bergisch-Gladbach, Germany) and anti-glucose transporter GLUT1 antibody AlexaFluor® 488 (clone: EPR3915, Abcam, Cambridge, UK). After washing samples were recorded on a FACS Canto II (BD Bioscience, Franklin Lakes, NJ).

Extracellular flux analysis. Bioenergetics were analyzed using a Seahorse XFe96 (Agilent, Santa Clara, CA) as previously described (Bottcher et al., 2018). Briefly, 3 x 10^4 fibroblasts were seeded per well in heptaplicates into Seahorse XF culture plates and incubated overnight at 37°C, 5%CO_2. Next day, medium was replaced by glucose-free (glycolysis stress test, GST) or glucose-containing DMEM (mitochondrial stress test, MST) with tightly adjusted pH and samples were incubated an additional 1 h in a CO_2-free atmosphere. Samples' extracellular acidification rate (ECAR) and oxygen consumption rate (OCR) were recorded after sequential injection of glucose, oligomycin, and 2-DG for the GST or oligomycin, FCCP, and antimycin A/rotenone for the MST. Last, total protein content per well was determined using the Pierce™ BCA Protein Assay Kit (Thermo Fisher Scientific, Waltham, MA) to normalize the recorded raw data. Resulting data was converted to csv-files using the Wave Desktop

Software and metabolic parameters were calculated with Microsoft Excel. GraphPad Prism 8 was used for visualization and statistical analysis.

Treatment with 2-Deoxy-D-glucose (2-DG) *in vitro* and *in vivo*

For inhibition of glycolysis *in vitro*, isolated fibroblasts were cultured with 2mM 2-DG (Sigma Aldrich) for 24 h at 37°C, 5% CO_2. For inhibition of glycolysis in vivo, C57BL/6 WT mice received 2 mM 2-DG in their drinking water. 2-DG treatment was begun one day before the induction of arthritis by injection of MSU crystals and continued until the end of the experiment.

Cell sorting of fibroblasts by flow cytometry

Cultured cells were detached at passage 2 from flasks by Corning™ Cell stripper (Fisher scientific) and stained in FACS buffer (PBS, 10% FCS, 0.5 mM EDTA) with a PerCP Cy5.5 or an APC-conjugated anti-CD45 antibody (Biolegend 103132 and 103112), a BV421-conjugated anti-CD31 antibody (Biolegend, 102423) and Sytox Green (Thermofisher S7020). After washing Sytox Green$^+$ (dead) cells, CD45$^+$ and CD31$^+$ cells were sorted out on a FACS Aria machine. CD45$^-$CD31$^-$ remaining fibroblasts were used after re-culturing.

Scanning electron microscopy

10,000 mouse fibroblasts were cultured for 24h in plastic flat-bottomed 96-well plates precoated with 50 µg/ml fibronectin over night at 4°C. After fixation with 0.1 M 4-(2-hydroxyethyl)-1-piperazineethanesulfonic acid (HEPES) buffer (pH 7.2) containing 0.01 M CaCl2, 0.01 M MgCl2, 0.09 M saccharose, and 2% glutaraldehyde as a fixative, samples were dehydrated in an ascending ethanol series (2 × 10 min 30% EtOH, 1 × 10 min 50% EtOH, 1 × 10 min 70% EtOH, 3 × 10 min 100% EtOH), followed by 2 × 5 min incubation with 99.9% hexamethyldisilazane ReagentPlusR (MilliporeSigma, Burlington, MA, USA) and evaporation/air drying overnight as described (Nation, 1983). Subsequently, the base of the well was carefully punched out including the cell layer, attached on stubs for electron microscopy, and sputter-coated with Au (Emitech K575X; Quorum Technologies, Laughton, United Kingdom), 2 × 15 mA, 60 s. The samples were then examined using a Tescan Lyra3 field-emitting scanning electron microscope at 5 kV accelerating voltage.

Bone marrow transplantation

6 weeks old C57BL/6 Complement C3-deficient CD45.2$^+$ recipient mice were irradiated with a total of 10 Gray at the department of Radiation oncology, University of Erlangen, and reconstituted 2 hours afterwards intravenously with 5x10^6 bone marrow cells isolated from CD45.1$^+$ C57BL/6 WT donor mice. 6 weeks after transplantation, bone marrow chimerism was verified by detecting CD45.1$^+$ and CD45.2$^+$ cells in the peripheral blood of recipient mice by flow cytometry, using a PE-Cy7-labelled anti CD45.1 and an AlexaFluor700-labelled antiCD45.2 antibody (both from eBioscience), respectively.

Osteoclast differentiation

Bone marrow cells were isolated from tibia and femur of 8-week-old Balb/C mice as described elsewhere (Steffen et al., 2019). After lysis of erythrocytes with erylysis buffer (155 nM NH_4Cl, 10 mM $KHCO_3$, 0.1 mM EDTA, pH 7), cells were cultured for 24 hours in αMEM supplemented with 10% FCS and 1% Penicillin-Streptomycin. Non-adherent cells (200 x 10^3 well) were added to 96 well plates and co-cultured with naïve, -/MSU or MSU/MSU fibroblasts (1 x10^4/well) in αMEM supplemented with 10% FCS, 1% Penicillin-Streptomycin, 30 ng/ml recombinant murine M-CSF (PeproTech, 315-02) and 10 ng/ml recombinant murine RANKL (PeproTech 315-11). In some experiments, the TNF inhibitor

etanercept (Enbrel, Pfizer; 25 µg/ml), the Il-1 antagonist Anakinra (Kineret, SOBI; 20 µg/ml) or recombinant osteoprotegerin (Peprotech; 20 ng/ml), the decoy receptor of RANKL, were added. After 5 days, cells were fixed and stained for TRAP activity using a commercially available kit (Sigma, 387A-1KT). TRAP-positive multinucleated cells designated as osteoclasts were counted by light microscopy and number of nuclei was determined. Total area covered by osteoclasts was determined by Adobe Photoshop CS6 software.

Determination of RANKL and OPG concentrations in fibroblast-derived supernatants

Mouse fibroblasts were incubated in 96 well-plates in 200 µl culture medium with or without 2 mM 2-DG for 24 hours. Concentrations of RANKL and OPG in supernatants were then determined by Mouse TRANCE/RANKL Duoset (R&D Systems #DY462) and Mouse Osteoprotegrin Duo set (R&D Systems #DY459) ELISA, respectively, according to the manufacturer´s instructions.

Induction of inflammatory memory by injection of fibroblasts into the paw

Left paws of mice were injected with MSU crystals. After the resolution of the inflammation, 500 x 10^3 sorted cells were transferred to contralateral paws by subcutaneous injection between the metatarsals. After two days, arthritis was initiated in both paws by the injection of MSU crystals.

Inflammasome inactivation

Balb/C mice received intraperitoneal injections of 10 mg/kg MCC950 (Sigma Aldrich PZ0280) or sterile PBS (vehicle) 2 days before the MSU crystal injection. Treatment was continued every second day until the end of the experiment.

Optical clearing of mouse knee samples

ColVIcreR26-tdTomato mice were intravenously administered 2.5 µg Alexa Fluor 647 anti-mouse Ly6G antibody (Biolegend, 127610) in PBS and sacrificed after 1 hour. Perfusion was performed using 5 mM EDTA in PBS and fixation was carried out by perfusion of 4% PFA/PBS (pH = 7.4). Hind limbs were cut and surrounding skin and muscles were removed. Knee joints were fixed in 4% PFA (pH 7.4) for 4 hours at 4°C. Tissue dehydration was done by immersing samples in a series of ethanol solutions: 50%, 70% and two consecutive incubations with 100% ethanol at 4°C for 12h each. Mice knee samples were transferred to ethyl cinnamate and incubated at room temperature for 6h.

Light sheet fluorescence microscopy (LSFM)

LSFM of optically cleared mouse knee joints was performed with a LaVison BioTec Ultramicroscope II including an Olympus MVX10 zoom body (Olympus), a LaVision BioTec Laser Module, and an Andor Neo sCMOS Camera with a pixel size of 6.5 µm. For visualization of general tissue morphology, a 488-nm optically pumped semiconductor laser (OPSL) was used to generate autofluorescent signals. For tdTomato excitation, a 561-nm OPSL and for Ly6G-AF647 excitation, a 647-nm diode laser was used. Emitted wavelengths were detected with specific detection filters: 525/50 nm for autofluorescence, 620/60 nm for tdTomato, and 680/30 nm for Ly6G-AF647. The optical zoom factor of the measurements varied from 1.26 to 8 and the light-sheet thickness ranged from 5 to 10 µm.

3D surface rendering and quantification of lining integrity and cells in the sublining

3D reconstruction of LSFM-scanned mouse knee joints was performed using Imaris software (Version 9.3, Bitplane). The FIJI plugin “Calculator Plus“ was utilized to subtract the intensity adjusted autofluorescence (488-nm) from the tdTomato Signal (561-nm), improving the signal to noise ratio.

For analyzing the synovial lining integrity, the synovial lining was optically separated from the sublining tissue by semi-automated volumetric surface rendering. The ratio of tdTomato+ lining fibroblast volume to lining tissue volume was calculated and normalized against the mean of the -/- control group.
The number of tdTomato$^+$ cells in the synovial sublining tissue was quantified using the Imaris cell counter module with a size threshold of 5 µm.

RNAscope and immunohistochemistry for C3 and CD90 in human synovium

RNAscope was carried out on formalin fixed paraffin embedded osteoarthritis human synovium sections according to the manufacturer's protocol. C3 probe (430701) was utilised with the single-colour RNAscope 2.5 HD Assay Red kit (322360, both Bio-Techne). The slides were treated for 15 minutes with the Retrieval Buffer and incubated for 30 minutes with Protease Plus. Following the RNAscope colour development, the slides were washed in distilled water for 5 minutes and the immunohistochemistry protocol was started. In brief, sections were blocked with Bloxall Endogenous Peroxidase and Alkaline Phosphatase Blocking Solution (SP-6000, Vector Laboratories) for 10 minutes and with 10% normal horse serum (H0146, Sigma-Aldrich) Tris buffer for 10 minutes. The sections were then incubated with sheep anti-human CD90 primary antibody (AF2067, R&D Systems) at a dilution of 1:100 at 4°C overnight, followed by incubation with donkey anti-sheep HRP (713-035-147, Jackson Immuno Research), and colour development with ImmPACT DAB Peroxidase (HRP) Substrate (SK-4105, Vector Laboratories). The nuclei were stained with Vector Hematoxylin QS (H-3404) and slides were mounted in VectaMount Permanent Mounting Medium (H-5000, both Vector Laboratories). The slides were visualised using Zeiss Axio Scan and analysed in Zen Blue (both Zeiss).

Confocal microscopy for detection of complement C3 and C3aR expression and inflammasome activation

For C3 expression analysis, cells were adhered to poly-Lysine slides and fixed with paraformaldehyde (2%), treated with Triton X-100 (Sigma, 0.3%, 10 min on ice) and incubated with anti-C3 (clone: 11H9, Abcam) and anti-mto (clone: D95F2, Cell Signaling Technology) overnight at 4°C in a humid chamber. After incubation with anti-rat IgG F(ab')2 Fragment Alexa 488 conjugate and anti-rabbit IgG F(ab')2 Fragment 674 conjugate (2 hours, 4°C in a humid chamber), DAPI (1 µg/ml) was added during the last 10 min. In some experiments cells were stained with phalloidin (Flash Phalloidin™ Red 594, BioLegend) according to the manufacturer's instructions. Slides were analyzed by confocal microscopy (LSM700, Zeiss) at x630 magnification.

C3aR expression analysis

Caspase-1 activity was detected using the FLICA® 660 Caspase-1 assay kit from ImmunoChemistry Technologies (Bloomington, USA) according to the manufacturer's instructions. Cells were washed with PBS and incubated with the FLICA® 660-YVAD-fmk reagent (1:150, 30 min) at 37 °C and 5 % CO2. After this, cells were adhered to poly-Lysine slides and fixed with paraformaldehyde (2%). Cells were stained with DAPI and phalloidin (Flash Phalloidin™ Red 594, BioLegend) according to the manufacturer's instructions. Slides were analyzed by confocal microscopy (LSM700, Zeiss) at x630 magnification.

Nociception analysis

Tests for mechanical allodynia were performed using a dynamic plantar aesthesiometer (Model 37450, Ugo Basile, Varese, Italy) according to Von Frey. The animals were habituated to the test situation (wire mesh base plate with 10 x 10 cm transparent animal enclosures, sides neighboring two animals were

covered) for 2 h prior to testing. Performing the test, a blunt 0.5 mm Von Frey-type filament exerted an increasing force of 0.2 g/s until the animal twitched or lifted the paw, or until the cut-off value of 8 g was reached. Both paws were tested alternately, with at least 5 min pause between two tests of the same paw. Per animal and paw, 4 tests were performed, and exerted force (g) and paw withdrawal latency (s) were averaged per animal.

Statistical analysis

Two group comparisons were performed using unpaired or paired 2-tailed Student's t-test or, in the case of non-normally distributed data, by 2-tailed Mann-Whitney U test. Gaussian distribution of samples was checked using D'Agostino-Pearson omnibus normality test. Within each set of experiments shown in one graph multiple comparisons of groups were performed by ANOVA and adjusted using Tukey's multiple comparisons test or Dunnett's test if several values were compared to a control value. In case of non-normally distributed data we used Kruskal-Wallis test with Dunn's post-hoc test for multiple comparisons. Adjusted p-values < 0.05 were considered statistically significant. Computations and charts were performed using GraphPad Prism 8.3 software.

Supplemental table legends

Table S1. Canonical pathways in naïve (-/-), non-**primed (-/MSU) and primed (MSU/MSU) fibroblasts identified by Ingenuity pathway analysis.**

Table S2. Canonical pathways and upstream regulators in a confirmation set of non-primed (-/MSU) and primed (MSU/MSU) fibroblasts identified by Ingenuity pathway analysis.

Table S3. Cluster marker genes identified for the clusters of single cells shown in Figure 3H.

Table S4. Characteristics of individuals with arthritis and normal healthy controls enrolled in the study.

Acknowledgements

This work was supported by the Deutsche Forschungsgemeinschaft (DFG – FG 2886 "PANDORA" – TP04 to U. Steffen, TP08 to J. Friščić, S.-J. Popp, D. Mougiakakos and M.H. Hoffmann, Z-project (A. Kleyer); CRC1181-B03/Z2 to M.H. Hoffmann and T. Bäuerle, respectively), the European Union (ERC Synergy grant 810316 4DnanoSCOPE to G. Schett), the EU/EFPIA Innovative Medicines Initiative 1 Joint Undertaking BTCure under grant agreement no 115142, and the EU/EFPIA Innovative Medicines Initiative 2 Joint Undertaking RTCure grant no. 777357. X. Chen was supported by a grant from the Chinese Scholarship Council. We thank the Optical imaging center Erlangen (OICE), the Precinical imaging platform Erlangen (PIPE), and Uwe Appelt from the core unit for cell sorting and immunomonitoring at the Nikolaus-Fiebiger-Center for Molecular Medicine Erlangen, and Heike Danzer, Institute of Genetics, University of Erlangen-Nuremberg for technical assistance. We further thank Fabian Hartmann for collation of clinical characteristics of patients included in the study, Martin Göksu for recruitment of human synovial tissue for fibroblast isolation, Denise Beckmann for help with setting up the MATRIN assay, Karolina von Dalwigk, Adela Rauschenberg and Lisa Möller for technical help with functional analysis of fibroblasts. We also thank G. Kollias, BSRC Alexander Fleming, for allowing us to use *ColVI*^{cre} mice.

Author contributions

Conceptualization, J.F., M.B., H.B., M.H., H.P.K., U.S., A.G., K.K., A.F., C.D.B., G.S., D.M and M.H.H.; Methodology, J.F., C.R., M.B., B.W., H.B., K.I.W., T.M., O.A., F.T.A., A.K.-P., I.W., A.H., H.P.K., B.F., L.K., U.S., T.B., A.G., K.K. and M.H.H.; Software, O.A.; Formal analysis, M.B., J.T., H.Z., P.K., K.R., D.M. and M.H.H.; Investigation, J.F., C.R., M.B., B.W., H.B., S-J.P., D.W., A.F., F.T.A., M.E., Z.S., I.W., B.F., and L.K.; Resources, V.T., G.S., K.R., A.K., J.D., T.B., J.K., K.K., A.F., and C.D.B.; Data Curation, K.R.; Writing – Original Draft, M.H.H.; Writing, Review & Editing, M.B., A.F., J.K., C.D.B, G.S., D.M. and M.H.H.; Visualization, J.F., C.R., M.B., J.T., H.B., T.M., A.G., and M.H.H.; Supervision and Project Administration, M.H.H.; Funding Acquisition, K.K., G.S., C.D.B, D.M. and M.H.H.

Competing interests

The authors declare no competing interests.

References

Akins, N.S., Nielson, T.C., and Le, H.V. (2018). Inhibition of Glycolysis and Glutaminolysis: An Emerging Drug Discovery Approach to Combat Cancer. Curr Top Med Chem *18*, 494-504.

Alivernini, S., MacDonald, L., Elmesmari, A., Finlay, S., Tolusso, B., Gigante, M.R., Petricca, L., Di Mario, C., Bui, L., Perniola, S.*, et al.* (2020). Distinct synovial tissue macrophage subsets regulate inflammation and remission in rheumatoid arthritis. Nature medicine *26*, 1295-1306.

An, L.L., Mehta, P., Xu, L., Turman, S., Reimer, T., Naiman, B., Connor, J., Sanjuan, M., Kolbeck, R., and Fung, M. (2014). Complement C5a potentiates uric acid crystal-induced IL-1beta production. European journal of immunology *44*, 3669-3679.

Araki, Y., Tsuzuki Wada, T., Aizaki, Y., Sato, K., Yokota, K., Fujimoto, K., Kim, Y.T., Oda, H., Kurokawa, R., and Mimura, T. (2016). Histone Methylation and STAT-3 Differentially Regulate Interleukin-6-Induced Matrix Metalloproteinase Gene Activation in Rheumatoid Arthritis Synovial Fibroblasts. Arthritis Rheumatol *68*, 1111-1123.

Arbore, G., and Kemper, C. (2016). A novel "complement-metabolism-inflammasome axis" as a key regulator of immune cell effector function. European journal of immunology *46*, 1563-1573.

Arbore, G., Kemper, C., and Kolev, M. (2017). Intracellular complement - the complosome - in immune cell regulation. Molecular immunology *89*, 2-9.

Arbore, G., West, E.E., Spolski, R., Robertson, A.A.B., Klos, A., Rheinheimer, C., Dutow, P., Woodruff, T.M., Yu, Z.X., O'Neill, L.A.*, et al.* (2016). T helper 1 immunity requires complement-driven NLRP3 inflammasome activity in CD4(+) T cells. Science *352*, aad1210.

Armaka, M., Apostolaki, M., Jacques, P., Kontoyiannis, D.L., Elewaut, D., and Kollias, G. (2008). Mesenchymal cell targeting by TNF as a common pathogenic principle in chronic inflammatory joint and intestinal diseases. The Journal of experimental medicine *205*, 331-337.

Arnett, F.C., Edworthy, S.M., Bloch, D.A., McShane, D.J., Fries, J.F., Cooper, N.S., Healey, L.A., Kaplan, S.R., Liang, M.H., Luthra, H.S., and et al. (1988). The American Rheumatism Association 1987 revised criteria for the classification of rheumatoid arthritis. Arthritis and rheumatism *31*, 315-324.

Asgari, E., Le Friec, G., Yamamoto, H., Perucha, E., Sacks, S.S., Kohl, J., Cook, H.T., and Kemper, C. (2013). C3a modulates IL-1beta secretion in human monocytes by regulating ATP efflux and subsequent NLRP3 inflammasome activation. Blood *122*, 3473-3481.

Bartok, B., and Firestein, G.S. (2010). Fibroblast-like synoviocytes: key effector cells in rheumatoid arthritis. Immunol Rev *233*, 233-255.

Baxter, A.G., and Cooke, A. (1993). Complement lytic activity has no role in the pathogenesis of autoimmune diabetes in NOD mice. Diabetes *42*, 1574-1578.

Bosma, G.C., Davisson, M.T., Ruetsch, N.R., Sweet, H.O., Shultz, L.D., and Bosma, M.J. (1989). The mouse mutation severe combined immune deficiency (scid) is on chromosome 16. Immunogenetics *29*, 54-57.
Bottcher, M., Renner, K., Berger, R., Mentz, K., Thomas, S., Cardenas-Conejo, Z.E., Dettmer, K., Oefner, P.J., Mackensen, A., Kreutz, M., and Mougiakakos, D. (2018). D-2-hydroxyglutarate interferes with HIF-1alpha stability skewing T-cell metabolism towards oxidative phosphorylation and impairing Th17 polarization. Oncoimmunology *7*, e1445454.
Bottini, N., and Firestein, G.S. (2013). Duality of fibroblast-like synoviocytes in RA: passive responders and imprinted aggressors. Nat Rev Rheumatol *9*, 24-33.
Brackertz, D., Mitchell, G.F., and Mackay, I.R. (1977). Antigen-induced arthritis in mice. I. Induction of arthritis in various strains of mice. Arthritis and rheumatism *20*, 841-850.
Buckley, C.D. (2017). Why should rheumatologists care about fibroblasts?: Answering questions about tissue tropism and disease persistence. Rheumatology *56*, 863-864.
Buckley, C.D., Pilling, D., Lord, J.M., Akbar, A.N., Scheel-Toellner, D., and Salmon, M. (2001). Fibroblasts regulate the switch from acute resolving to chronic persistent inflammation. Trends in immunology *22*, 199-204.
Buenrostro, J.D., Wu, B., Chang, H.Y., and Greenleaf, W.J. (2015). ATAC-seq: A Method for Assaying Chromatin Accessibility Genome-Wide. Curr Protoc Mol Biol *109*, 21 29 21-21 29 29.
Bustamante, M.F., Oliveira, P.G., Garcia-Carbonell, R., Croft, A.P., Smith, J.M., Serrano, R.L., Sanchez-Lopez, E., Liu, X., Kisseleva, T., Hay, N.*, et al.* (2018). Hexokinase 2 as a novel selective metabolic target for rheumatoid arthritis. Annals of the rheumatic diseases *77*, 1636-1643.
Butler, A., Hoffman, P., Smibert, P., Papalexi, E., and Satija, R. (2018). Integrating single-cell transcriptomic data across different conditions, technologies, and species. Nat Biotechnol *36*, 411-420.
Cambre, I., Gaublomme, D., Burssens, A., Jacques, P., Schryvers, N., De Muynck, A., Meuris, L., Lambrecht, S., Carter, S., de Bleser, P.*, et al.* (2018). Mechanical strain determines the site-specific localization of inflammation and tissue damage in arthritis. Nature communications *9*, 4613.
Cambre, I., Gaublomme, D., Schryvers, N., Lambrecht, S., Lories, R., Venken, K., and Elewaut, D. (2019). Running promotes chronicity of arthritis by local modulation of complement activators and impairing T regulatory feedback loops. Annals of the rheumatic diseases *78*, 787-795.
Carta, S., Penco, F., Lavieri, R., Martini, A., Dinarello, C.A., Gattorno, M., and Rubartelli, A. (2015). Cell stress increases ATP release in NLRP3 inflammasome-mediated autoinflammatory diseases, resulting in cytokine imbalance. Proceedings of the National Academy of Sciences of the United States of America *112*, 2835-2840.
Chang, S.K., Noss, E.H., Chen, M., Gu, Z., Townsend, K., Grenha, R., Leon, L., Lee, S.Y., Lee, D.M., and Brenner, M.B. (2011). Cadherin-11 regulates fibroblast inflammation. Proceedings of the National Academy of Sciences of the United States of America *108*, 8402-8407.
Chen, K., Zhang, J., Zhang, W., Zhang, J., Yang, J., Li, K., and He, Y. (2013). ATP-P2X4 signaling mediates NLRP3 inflammasome activation: a novel pathway of diabetic nephropathy. The international journal of biochemistry & cell biology *45*, 932-943.
Chen, X., Yu, Y., Mi, L.Z., Walz, T., and Springer, T.A. (2012). Molecular basis for complement recognition by integrin alphaXbeta2. Proceedings of the National Academy of Sciences of the United States of America *109*, 4586-4591.
Christensen, A.D., Haase, C., Cook, A.D., and Hamilton, J.A. (2016). K/BxN Serum-Transfer Arthritis as a Model for Human Inflammatory Arthritis. Front Immunol *7*, 213.
Cimmino, M.A., Zampogna, G., Parodi, M., Andracco, R., Barbieri, F., Paparo, F., Ferrero, G., and Garlaschi, G. (2011). MRI synovitis and bone lesions are common in acute gouty arthritis of the wrist even during the first attack. Annals of the rheumatic diseases *70*, 2238-2239.
Coll, R.C., Robertson, A.A., Chae, J.J., Higgins, S.C., Munoz-Planillo, R., Inserra, M.C., Vetter, I., Dungan, L.S., Monks, B.G., Stutz, A.*, et al.* (2015). A small-molecule inhibitor of the NLRP3 inflammasome for the treatment of inflammatory diseases. Nature medicine *21*, 248-255.

Coulthard, L.G., and Woodruff, T.M. (2015). Is the complement activation product C3a a proinflammatory molecule? Re-evaluating the evidence and the myth. Journal of immunology *194*, 3542-3548.
Croft, A.P., Campos, J., Jansen, K., Turner, J.D., Marshall, J., Attar, M., Savary, L., Wehmeyer, C., Naylor, A.J., Kemble, S.*, et al.* (2019). Distinct fibroblast subsets drive inflammation and damage in arthritis. Nature *570*, 246-251.
Croft, A.P., Naylor, A.J., Marshall, J.L., Hardie, D.L., Zimmermann, B., Turner, J., Desanti, G., Adams, H., Yemm, A.I., Muller-Ladner, U.*, et al.* (2016). Rheumatoid synovial fibroblasts differentiate into distinct subsets in the presence of cytokines and cartilage. Arthritis Res Ther *18*, 270.
Crowley, T., O'Neil, J.D., Adams, H., Thomas, A.M., Filer, A., Buckley, C.D., and Clark, A.R. (2017). Priming in response to pro-inflammatory cytokines is a feature of adult synovial but not dermal fibroblasts. Arthritis Res Ther *19*, 35.
Culemann, S., Gruneboom, A., Nicolas-Avila, J.A., Weidner, D., Lammle, K.F., Rothe, T., Quintana, J.A., Kirchner, P., Krljanac, B., Eberhardt, M.*, et al.* (2019). Locally renewing resident synovial macrophages provide a protective barrier for the joint. Nature *572*, 670-675.
Cumpelik, A., Ankli, B., Zecher, D., and Schifferli, J.A. (2016). Neutrophil microvesicles resolve gout by inhibiting C5a-mediated priming of the inflammasome. Annals of the rheumatic diseases *75*, 1236-1245.
Czegley, C., Gillmann, C., Schauer, C., Seyler, L., Reinwald, C., Hahn, M., Uder, M., Jochmann, K., Naschberger, E., Stock, M.*, et al.* (2018). A model of chronic enthesitis and new bone formation characterized by multimodal imaging. Dis Model Mech *11*.
De Maesschalck, R., Jouan-Rimbaud, D., and Massart, D.L. (2000). The Mahalanobis distance. Chemometrics Intellig Lab Syst *50*, 1-18.
Del Rey, M.J., Valin, A., Usategui, A., Garcia-Herrero, C.M., Sanchez-Arago, M., Cuezva, J.M., Galindo, M., Bravo, B., Canete, J.D., Blanco, F.J.*, et al.* (2017). Hif-1alpha Knockdown Reduces Glycolytic Metabolism and Induces Cell Death of Human Synovial Fibroblasts Under Normoxic Conditions. Sci Rep *7*, 3644.
Dominguez-Andres, J., Fanucchi, S., Joosten, L.A.B., Mhlanga, M.M., and Netea, M.G. (2020). Advances in understanding molecular regulation of innate immune memory. Curr Opin Cell Biol *63*, 68-75.
Donlin, L.T., Rao, D.A., Wei, K., Slowikowski, K., McGeachy, M.J., Turner, J.D., Meednu, N., Mizoguchi, F., Gutierrez-Arcelus, M., Lieb, D.J.*, et al.* (2018). Methods for high-dimensional analysis of cells dissociated from cryopreserved synovial tissue. Arthritis Res Ther *20*, 139.
Eng, S.W.M., Aeschlimann, F.A., van Veenendaal, M., Berard, R.A., Rosenberg, A.M., Morris, Q., Yeung, R.S.M., and Re, A.-O.R.C. (2019). Patterns of joint involvement in juvenile idiopathic arthritis and prediction of disease course: A prospective study with multilayer non-negative matrix factorization. PLoS Med *16*, e1002750.
Falconer, J., Murphy, A.N., Young, S.P., Clark, A.R., Tiziani, S., Guma, M., and Buckley, C.D. (2018). Review: Synovial Cell Metabolism and Chronic Inflammation in Rheumatoid Arthritis. Arthritis Rheumatol *70*, 984-999.
Fearon, U., Canavan, M., Biniecka, M., and Veale, D.J. (2016). Hypoxia, mitochondrial dysfunction and synovial invasiveness in rheumatoid arthritis. Nat Rev Rheumatol *12*, 385-397.
Filer, A., Ward, L.S.C., Kemble, S., Davies, C.S., Munir, H., Rogers, R., Raza, K., Buckley, C.D., Nash, G.B., and McGettrick, H.M. (2017). Identification of a transitional fibroblast function in very early rheumatoid arthritis. Annals of the rheumatic diseases *76*, 2105-2112.
Folmes, C.D., Dzeja, P.P., Nelson, T.J., and Terzic, A. (2012). Metabolic plasticity in stem cell homeostasis and differentiation. Cell Stem Cell *11*, 596-606.
Fromm, S., Cunningham, C.C., Dunne, M.R., Veale, D.J., Fearon, U., and Wade, S.M. (2019). Enhanced angiogenic function in response to fibroblasts from psoriatic arthritis synovium compared to rheumatoid arthritis. Arthritis Res Ther *21*, 297.
Gallagher, L., Cregan, S., Biniecka, M., Cunningham, C., Veale, D.J., Kane, D.J., Fearon, U., and Mullan, R.H. (2019). Insulin Resistant Pathways are associated with Disease Activity in Rheumatoid Arthritis

and are Subject to Disease Modification through Metabolic Reprogramming; A Potential Novel Therapeutic Approach. Arthritis Rheumatol.
Garcia-Carbonell, R., Divakaruni, A.S., Lodi, A., Vicente-Suarez, I., Saha, A., Cheroutre, H., Boss, G.R., Tiziani, S., Murphy, A.N., and Guma, M. (2016). Critical Role of Glucose Metabolism in Rheumatoid Arthritis Fibroblast-like Synoviocytes. Arthritis Rheumatol *68*, 1614-1626.
Heremans, H., Van Damme, J., Dillen, C., Dijkmans, R., and Billiau, A. (1990). Interferon gamma, a mediator of lethal lipopolysaccharide-induced Shwartzman-like shock reactions in mice. The Journal of experimental medicine *171*, 1853-1869.
Holers, V.M., and Banda, N.K. (2018). Complement in the Initiation and Evolution of Rheumatoid Arthritis. Front Immunol *9*, 1057.
Hu, F., Liu, H., Xu, L., Li, Y., Liu, X., Shi, L., Su, Y., Qiu, X., Zhang, X., Yang, Y.*, et al.* (2016). Hypoxia-inducible factor-1alpha perpetuates synovial fibroblast interactions with T cells and B cells in rheumatoid arthritis. European journal of immunology *46*, 742-751.
Huber, R., Bikker, R., Welz, B., Christmann, M., and Brand, K. (2017). TNF Tolerance in Monocytes and Macrophages: Characteristics and Molecular Mechanisms. J Immunol Res *2017*, 9570129.
Humbles, A.A., Lu, B., Nilsson, C.A., Lilly, C., Israel, E., Fujiwara, Y., Gerard, N.P., and Gerard, C. (2000). A role for the C3a anaphylatoxin receptor in the effector phase of asthma. Nature *406*, 998-1001.
Ignatius, A., Schoengraf, P., Kreja, L., Liedert, A., Recknagel, S., Kandert, S., Brenner, R.E., Schneider, M., Lambris, J.D., and Huber-Lang, M. (2011). Complement C3a and C5a modulate osteoclast formation and inflammatory response of osteoblasts in synergism with IL-1beta. J Cell Biochem *112*, 2594-2605.
Irmscher, S., Doring, N., Halder, L.D., Jo, E.A.H., Kopka, I., Dunker, C., Jacobsen, I.D., Luo, S., Slevogt, H., Lorkowski, S.*, et al.* (2018). Kallikrein Cleaves C3 and Activates Complement. J Innate Immun *10*, 94-105.
Kataoka, S., Satoh, J., Fujiya, H., Toyota, T., Suzuki, R., Itoh, K., and Kumagai, K. (1983). Immunologic aspects of the nonobese diabetic (NOD) mouse. Abnormalities of cellular immunity. Diabetes *32*, 247-253.
Katz, Y., and Strunk, R.C. (1988). Synovial fibroblast-like cells synthesize seven proteins of the complement system. Arthritis and rheumatism *31*, 1365-1370.
Khameneh, H.J., Ho, A.W., Laudisi, F., Derks, H., Kandasamy, M., Sivasankar, B., Teng, G.G., and Mortellaro, A. (2017). C5a Regulates IL-1beta Production and Leukocyte Recruitment in a Murine Model of Monosodium Urate Crystal-Induced Peritonitis. Front Pharmacol *8*, 10.
Kiener, H.P., Niederreiter, B., Lee, D.M., Jimenez-Boj, E., Smolen, J.S., and Brenner, M.B. (2009). Cadherin 11 promotes invasive behavior of fibroblast-like synoviocytes. Arthritis and rheumatism *60*, 1305-1310.
Kiener, H.P., Watts, G.F., Cui, Y., Wright, J., Thornhill, T.S., Skold, M., Behar, S.M., Niederreiter, B., Lu, J., Cernadas, M.*, et al.* (2010). Synovial fibroblasts self-direct multicellular lining architecture and synthetic function in three-dimensional organ culture. Arthritis Rheum *62*, 742-752.
Kienhofer, D., Hahn, J., Schubert, I., Reinwald, C., Ipseiz, N., Lang, S.C., Borras, E.B., Amann, K., Sjowall, C., Barron, A.E.*, et al.* (2014). No evidence of pathogenic involvement of cathelicidins in patient cohorts and mouse models of lupus and arthritis. PLoS One *9*, e115474.
King, B.C., Kulak, K., Krus, U., Rosberg, R., Golec, E., Wozniak, K., Gomez, M.F., Zhang, E., O'Connell, D.J., Renstrom, E., and Blom, A.M. (2019). Complement Component C3 Is Highly Expressed in Human Pancreatic Islets and Prevents beta Cell Death via ATG16L1 Interaction and Autophagy Regulation. Cell Metab *29*, 202-210 e206.
Klein, K., Frank-Bertoncelj, M., Karouzakis, E., Gay, R.E., Kolling, C., Ciurea, A., Bostanci, N., Belibasakis, G.N., Lin, L.L., Distler, O.*, et al.* (2017). The epigenetic architecture at gene promoters determines cell type-specific LPS tolerance. J Autoimmun *83*, 122-133.
Kolev, M., Dimeloe, S., Le Friec, G., Navarini, A., Arbore, G., Povoleri, G.A., Fischer, M., Belle, R., Loeliger, J., Develioglu, L.*, et al.* (2015). Complement Regulates Nutrient Influx and Metabolic Reprogramming during Th1 Cell Responses. Immunity *42*, 1033-1047.

Krenn, V., Morawietz, L., Haupl, T., Neidel, J., Petersen, I., and Konig, A. (2002). Grading of chronic synovitis--a histopathological grading system for molecular and diagnostic pathology. Pathol Res Pract *198*, 317-325.
Kubota, K., Ito, K., Morooka, M., Mitsumoto, T., Kurihara, K., Yamashita, H., Takahashi, Y., and Mimori, A. (2009). Whole-body FDG-PET/CT on rheumatoid arthritis of large joints. Ann Nucl Med *23*, 783-791.
Laudisi, F., Spreafico, R., Evrard, M., Hughes, T.R., Mandriani, B., Kandasamy, M., Morgan, B.P., Sivasankar, B., and Mortellaro, A. (2013). Cutting edge: the NLRP3 inflammasome links complement-mediated inflammation and IL-1beta release. Journal of immunology *191*, 1006-1010.
Laumonnier, Y., Karsten, C.M., and Kohl, J. (2017). Novel insights into the expression pattern of anaphylatoxin receptors in mice and men. Molecular immunology *89*, 44-58.
Lee, D.M., Kiener, H.P., Agarwal, S.K., Noss, E.H., Watts, G.F., Chisaka, O., Takeichi, M., and Brenner, M.B. (2007). Cadherin-11 in synovial lining formation and pathology in arthritis. Science *315*, 1006-1010.
Liszewski, M.K., Kolev, M., Le Friec, G., Leung, M., Bertram, P.G., Fara, A.F., Subias, M., Pickering, M.C., Drouet, C., Meri, S*., et al.* (2013). Intracellular complement activation sustains T cell homeostasis and mediates effector differentiation. Immunity *39*, 1143-1157.
Lories, R.J., Derese, I., De Bari, C., and Luyten, F.P. (2003). In vitro growth rate of fibroblast-like synovial cells is reduced by methotrexate treatment. Annals of the rheumatic diseases *62*, 568-571.
Love, M.I., Huber, W., and Anders, S. (2014). Moderated estimation of fold change and dispersion for RNA-seq data with DESeq2. Genome Biol *15*, 550.
Lubbers, R., van Essen, M.F., van Kooten, C., and Trouw, L.A. (2017). Production of complement components by cells of the immune system. Clin Exp Immunol *188*, 183-194.
Markiewski, M.M., Nilsson, B., Ekdahl, K.N., Mollnes, T.E., and Lambris, J.D. (2007). Complement and coagulation: strangers or partners in crime? Trends in immunology *28*, 184-192.
Martinon, F., Petrilli, V., Mayor, A., Tardivel, A., and Tschopp, J. (2006). Gout-associated uric acid crystals activate the NALP3 inflammasome. Nature *440*, 237-241.
Mastellos, D.C., Ricklin, D., and Lambris, J.D. (2019). Clinical promise of next-generation complement therapeutics. Nat Rev Drug Discov *18*, 707-729.
Maueroder, C., Kienhofer, D., Hahn, J., Schauer, C., Manger, B., Schett, G., Herrmann, M., and Hoffmann, M.H. (2015). How neutrophil extracellular traps orchestrate the local immune response in gout. J Mol Med (Berl) *93*, 727-734.
McGarry, T., Biniecka, M., Gao, W., Cluxton, D., Canavan, M., Wade, S., Wade, S., Gallagher, L., Orr, C., Veale, D.J., and Fearon, U. (2017). Resolution of TLR2-induced inflammation through manipulation of metabolic pathways in Rheumatoid Arthritis. Sci Rep *7*, 43165.
McInnes, I.B., and Schett, G. (2011). The pathogenesis of rheumatoid arthritis. N Engl J Med *365*, 2205-2219.
Mizoguchi, F., Slowikowski, K., Wei, K., Marshall, J.L., Rao, D.A., Chang, S.K., Nguyen, H.N., Noss, E.H., Turner, J.D., Earp, B.E*., et al.* (2018). Functionally distinct disease-associated fibroblast subsets in rheumatoid arthritis. Nature communications *9*, 789.
Montero-Melendez, T., Nagano, A., Chelala, C., Filer, A., Buckley, C.D., and Perretti, M. (2020). Therapeutic senescence via GPCR activation in synovial fibroblasts facilitates resolution of arthritis. Nature communications *11*, 745.
Moon, J.S., Hisata, S., Park, M.A., DeNicola, G.M., Ryter, S.W., Nakahira, K., and Choi, A.M.K. (2015). mTORC1-Induced HK1-Dependent Glycolysis Regulates NLRP3 Inflammasome Activation. Cell reports *12*, 102-115.
Narita, T., Yin, S., Gelin, C.F., Moreno, C.S., Yepes, M., Nicolaou, K.C., and Van Meir, E.G. (2009). Identification of a novel small molecule HIF-1alpha translation inhibitor. Clin Cancer Res *15*, 6128-6136.
Nation, J.L. (1983). A new method using hexamethyldisilazane for preparation of soft insect tissues for scanning electron microscopy. Stain Technol *58*, 347-351.

Netea, M.G., Quintin, J., and van der Meer, J.W. (2011). Trained immunity: a memory for innate host defense. Cell Host Microbe *9*, 355-361.
Neumann, E., Barnum, S.R., Tarner, I.H., Echols, J., Fleck, M., Judex, M., Kullmann, F., Mountz, J.D., Scholmerich, J., Gay, S., and Muller-Ladner, U. (2002). Local production of complement proteins in rheumatoid arthritis synovium. Arthritis and rheumatism *46*, 934-945.
Newman, A.M., Steen, C.B., Liu, C.L., Gentles, A.J., Chaudhuri, A.A., Scherer, F., Khodadoust, M.S., Esfahani, M.S., Luca, B.A., Steiner, D*., et al.* (2019). Determining cell type abundance and expression from bulk tissues with digital cytometry. Nat Biotechnol *37*, 773-782.
Nguyen, H.N., Noss, E.H., Mizoguchi, F., Huppertz, C., Wei, K.S., Watts, G.F.M., and Brenner, M.B. (2017). Autocrine Loop Involving IL-6 Family Member LIF, LIF Receptor, and STAT4 Drives Sustained Fibroblast Production of Inflammatory Mediators. Immunity *46*, 220-232.
Nomoto, H., Pei, L., Montemurro, C., Rosenberger, M., Furterer, A., Coppola, G., Nadel, B., Pellegrini, M., Gurlo, T., Butler, P.C., and Tudzarova, S. (2020). Activation of the HIF1alpha/PFKFB3 stress response pathway in beta cells in type 1 diabetes. Diabetologia *63*, 149-161.
Ospelt, C., Brentano, F., Rengel, Y., Stanczyk, J., Kolling, C., Tak, P.P., Gay, R.E., Gay, S., and Kyburz, D. (2008). Overexpression of toll-like receptors 3 and 4 in synovial tissue from patients with early rheumatoid arthritis: toll-like receptor expression in early and longstanding arthritis. Arthritis and rheumatism *58*, 3684-3692.
Ospelt, C., Gay, S., and Klein, K. (2017). Epigenetics in the pathogenesis of RA. Semin Immunopathol *39*, 409-419.
Ostuni, R., Piccolo, V., Barozzi, I., Polletti, S., Termanini, A., Bonifacio, S., Curina, A., Prosperini, E., Ghisletti, S., and Natoli, G. (2013). Latent enhancers activated by stimulation in differentiated cells. Cell *152*, 157-171.
Pearson, T., Markees, T.G., Serreze, D.V., Pierce, M.A., Marron, M.P., Wicker, L.S., Peterson, L.B., Shultz, L.D., Mordes, J.P., Rossini, A.A., and Greiner, D.L. (2003). Genetic disassociation of autoimmunity and resistance to costimulation blockade-induced transplantation tolerance in nonobese diabetic mice. Journal of immunology *171*, 185-195.
Peters, M.A., Wendholt, D., Striethol t, S., Frank, S., Pundt, N., Korb-Pap, A., Joosten, L.A., van den Berg, W.B., Kollias, G., Eckes, B., and Pap, T. (2012). The loss of alpha2beta1 integrin suppresses joint inflammation and cartilage destruction in mouse models of rheumatoid arthritis. Arthritis and rheumatism *64*, 1359-1368.
Postigo, A.A., Garcia-Vicuna, R., Laffon, A., and Sanchez-Madrid, F. (1993). The role of adhesion molecules in the pathogenesis of rheumatoid arthritis. Autoimmunity *16*, 69-76.
Retser, E., Schied, T., Skryabin, B.V., Vogl, T., Kanczler, J.M., Hamann, N., Niehoff, A., Hermann, S., Eisenblatter, M., Wachsmuth, L*., et al.* (2013). Doxycycline-induced expression of transgenic human tumor necrosis factor alpha in adult mice results in psoriasis-like arthritis. Arthritis and rheumatism *65*, 2290-2300.
Richette, P., and Bardin, T. (2010). Gout. Lancet *375*, 318-328.
Rosengren, S., Boyle, D.L., and Firestein, G.S. (2007). Acquisition, culture, and phenotyping of synovial fibroblasts. Methods Mol Med *135*, 365-375.
Ruan, B.H., Li, X., Winkler, A.R., Cunningham, K.M., Kuai, J., Greco, R.M., Nocka, K.H., Fitz, L.J., Wright, J.F., Pittman, D.D*., et al.* (2010). Complement C3a, CpG oligos, and DNA/C3a complex stimulate IFN-alpha production in a receptor for advanced glycation end product-dependent manner. Journal of immunology *185*, 4213-4222.
Schauer, C., Janko, C., Munoz, L.E., Zhao, Y., Kienhofer, D., Frey, B., Lell, M., Manger, B., Rech, J., Naschberger, E*., et al.* (2014). Aggregated neutrophil extracellular traps limit inflammation by degrading cytokines and chemokines. Nature medicine *20*, 511-517.
Schett, G. (2018). Physiological effects of modulating the interleukin-6 axis. Rheumatology *57*, ii43-ii50.
Schett, G., Emery, P., Tanaka, Y., Burmester, G., Pisetsky, D.S., Naredo, E., Fautrel, B., and van Vollenhoven, R. (2016). Tapering biologic and conventional DMARD therapy in rheumatoid arthritis: current evidence and future directions. Annals of the rheumatic diseases *75*, 1428-1437.

Schett, G., and Neurath, M.F. (2018). Resolution of chronic inflammatory disease: universal and tissue-specific concepts. Nature communications *9*, 3261.
Scott, D.L., Wolfe, F., and Huizinga, T.W. (2010). Rheumatoid arthritis. Lancet *376*, 1094-1108.
Seeley, J.J., and Ghosh, S. (2017). Molecular mechanisms of innate memory and tolerance to LPS. J Leukoc Biol *101*, 107-119.
Serreze, D.V., Gaedeke, J.W., and Leiter, E.H. (1993). Hematopoietic stem-cell defects underlying abnormal macrophage development and maturation in NOD/Lt mice: defective regulation of cytokine receptors and protein kinase C. Proceedings of the National Academy of Sciences of the United States of America *90*, 9625-9629.
Seya, T., Nomura, M., Murakami, Y., Begum, N.A., Matsumoto, M., and Nagasawa, S. (1998). CD46 (membrane cofactor protein of complement, measles virus receptor): structural and functional divergence among species (review). Int J Mol Med *1*, 809-816.
Shi, L.Z., Wang, R., Huang, G., Vogel, P., Neale, G., Green, D.R., and Chi, H. (2011). HIF1alpha-dependent glycolytic pathway orchestrates a metabolic checkpoint for the differentiation of TH17 and Treg cells. The Journal of experimental medicine *208*, 1367-1376.
Song, J.S., Kim, Y.J., Han, K.U., Yoon, B.D., and Kim, J.W. (2015). Zymosan and PMA activate the immune responses of Mutz3-derived dendritic cells synergistically. Immunol Lett *167*, 41-46.
Stebulis, J.A., Rossetti, R.G., Atez, F.J., and Zurier, R.B. (2005). Fibroblast-like synovial cells derived from synovial fluid. J Rheumatol *32*, 301-306.
Steffen, U., Andes, F.T., and Schett, G. (2019). Generation and Analysis of Human and Murine Osteoclasts. Curr Protoc Immunol *125*, e74.
Tannahill, G.M., Curtis, A.M., Adamik, J., Palsson-McDermott, E.M., McGettrick, A.F., Goel, G., Frezza, C., Bernard, N.J., Kelly, B., Foley, N.H.*, et al.* (2013). Succinate is an inflammatory signal that induces IL-1beta through HIF-1alpha. Nature *496*, 238-242.
Tatar, Z., Migne, C., Petera, M., Gaudin, P., Lequerre, T., Marotte, H., Tebib, J., Pujos Guillot, E., and Soubrier, M. (2016). Variations in the metabolome in response to disease activity of rheumatoid arthritis. BMC Musculoskelet Disord *17*, 353.
Tennant, D.A., Duran, R.V., and Gottlieb, E. (2010). Targeting metabolic transformation for cancer therapy. Nat Rev Cancer *10*, 267-277.
Trouw, L.A., Pickering, M.C., and Blom, A.M. (2017). The complement system as a potential therapeutic target in rheumatic disease. Nat Rev Rheumatol *13*, 538-547.
Tuncel, J., Haag, S., Hoffmann, M.H., Yau, A.C., Hultqvist, M., Olofsson, P., Backlund, J., Nandakumar, K.S., Weidner, D., Fischer, A.*, et al.* (2016). Animal Models of Rheumatoid Arthritis (I): Pristane-Induced Arthritis in the Rat. PLoS One *11*, e0155936.
Vergne-Salle, P., Leger, D.Y., Bertin, P., Treves, R., Beneytout, J.L., and Liagre, B. (2005). Effects of the active metabolite of leflunomide, A77 1726, on cytokine release and the MAPK signalling pathway in human rheumatoid arthritis synoviocytes. Cytokine *31*, 335-348.
Vergunst, C.E., Gerlag, D.M., Dinant, H., Schulz, L., Vinkenoog, M., Smeets, T.J., Sanders, M.E., Reedquist, K.A., and Tak, P.P. (2007). Blocking the receptor for C5a in patients with rheumatoid arthritis does not reduce synovial inflammation. Rheumatology *46*, 1773-1778.
Wei, K., Korsunsky, I., Marshall, J.L., Gao, A., Watts, G.F.M., Major, T., Croft, A.P., Watts, J., Blazar, P.E., Lange, J.*, et al.* (2020). Synovial fibroblast positional identity controlled by inductive Notch signaling underlies pathologic damage in inflammatory arthritis. Nature *in press*.
West, E.E., Kunz, N., and Kemper, C. (2020). Complement and human T cell metabolism: Location, location, location. Immunol Rev *295*, 68-81.
Wolf, J., Rose-John, S., and Garbers, C. (2014). Interleukin-6 and its receptors: a highly regulated and dynamic system. Cytokine *70*, 11-20.
Wunrau, C., Schnaeker, E.M., Freyth, K., Pundt, N., Wendholt, D., Neugebauer, K., Hansen, U., Pap, T., and Dankbar, B. (2009). Establishment of a matrix-associated transepithelial resistance invasion assay to precisely measure the invasive potential of synovial fibroblasts. Arthritis and rheumatism *60*, 2606-2611.

Yang, Y., Wang, H., Kouadir, M., Song, H., and Shi, F. (2019). Recent advances in the mechanisms of NLRP3 inflammasome activation and its inhibitors. Cell Death Dis *10*, 128.
Yona, S., Kim, K.W., Wolf, Y., Mildner, A., Varol, D., Breker, M., Strauss-Ayali, D., Viukov, S., Guilliams, M., Misharin, A.*, et al.* (2013). Fate mapping reveals origins and dynamics of monocytes and tissue macrophages under homeostasis. Immunity *38*, 79-91.
Young, S.P., Kapoor, S.R., Viant, M.R., Byrne, J.J., Filer, A., Buckley, C.D., Kitas, G.D., and Raza, K. (2013). The impact of inflammation on metabolomic profiles in patients with arthritis. Arthritis and rheumatism *65*, 2015-2023.
Zelek, W.M., Menzies, G.E., Brancale, A., Stockinger, B., and Morgan, B.P. (2020). Characterizing the original anti-C5 function-blocking antibody, BB5.1, for species specificity, mode of action and interactions with C5. Immunology.
Zhang, F., Wei, K., Slowikowski, K., Fonseka, C.Y., Rao, D.A., Kelly, S., Goodman, S.M., Tabechian, D., Hughes, L.B., Salomon-Escoto, K.*, et al.* (2019). Defining inflammatory cell states in rheumatoid arthritis joint synovial tissues by integrating single-cell transcriptomics and mass cytometry. Nature immunology *20*, 928-942.

Figures

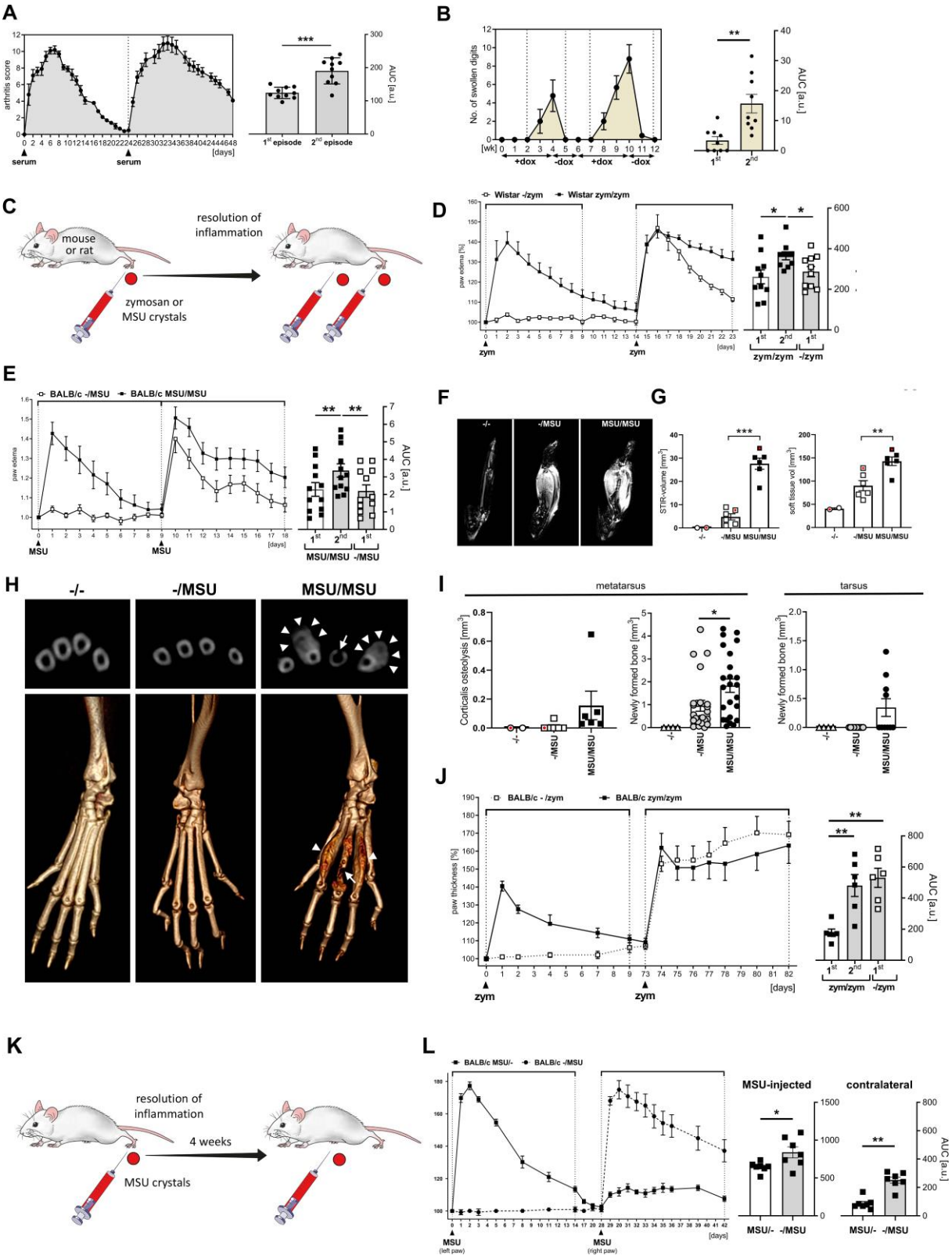

Figure 1. Repeated exposure to an inflammatory trigger causes prolonged and exacerbated course of inflammation and bone remodeling. (A) Course of clinical arthritis developing after repeated intraperitoneal injection of K/BxN serum. Shown are means and SEM (arthritis curve, left panel) and

individual values of areas under the curve (AUC) of the first and second episode of serum transfer arthritis (STA). N = 10. ***p < 0.001, as determined by paired t-test. **(B)** Digit swelling after repeated administration of doxycycline (dox) to inducible human TNF transgenic mice. Shown are means and SEM of the disease course and AUC of the first and second arthritis episode. N = 9. **p < 0.01, as determined by paired t-test. **(C)** Injection scheme of the inflammatory tissue priming model of arthritis. **(D)** Relative thickness of Wistar rat paws injected once (non-primed; -/zym) or twice (primed; zym/zym) with zymosan. Bar diagram shows means, SEM and individual values of AUC of the first and second arthritis episode in unprimed and primed paws. N = 10. *p < 0.05, repeated measures ANOVA with Tukey´s multiple comparisons test. **(E)** Swelling developing in paws of BALB/c mice injected once (non-primed; -/MSU) or twice (primed; MSU/MSU) with monosodium urate crystals. N = 12. **p < 0.01, repeated measures ANOVA with Tukeys´ multiple comparisons test. **(F, G)** Analysis of inflammation by magnetic resonance imaging (MRI) in non-injected paws of BALB/c mice (-/-), or 9 days after first/second injection of MSU crystals. **(F)** Increased tissue water content visualized as hyperintense areas on representative short tau inversion recovery (STIR) MR images. **(G)** Quantification of volumes of hyperintense areas (STIR volume) and soft-tissue volume from MRI. Samples shown in **(F)** are indicated with a red dot. **p < 0.01, ***p < 0.001, as determined by paired t-test. **(H)** Representative microcomputed tomography (µCT) slice images (upper panel) and 3D surface renderings (lower panels) in naïve paws and paws 9 days after first (non-primed) or second (primed) MSU crystal injection, respectively, showing osteolysis of the corticalis (white arrows) and newly formed bone (white arrowheads) in primed paws. **(I)** Volumes of areas of lowered bone density in the cortical bone of the metatarsus (N = 2-6) and of newly formed bone along the metatarsals (N = 4-24) and the tarsal area (N = 4-10), as evaluated by µCT. *p < 0.05, Mann Whitney U-test. **(J)** Development of paw swelling in BALB/c mice after an injection of zymosan in both paws 73 days after an initial zymosan injection into the left paw. Shown are means and SEM of arthritis curves and AUC. N = 6. **p < 0.01, as determined by repeated measures ANOVA with Tukey´s multiple comparisons test. **(K)** Injection scheme of the systemic inflammatory memory model of arthritis. **(L)** Arthritis curves and AUC after an injection of MSU crystals into the left paw followed by an injection into the right paw 28 days later. Shown are means and SEM. N = 7. *p < 0.05, **p < 0.01, as determined by paired t-test.

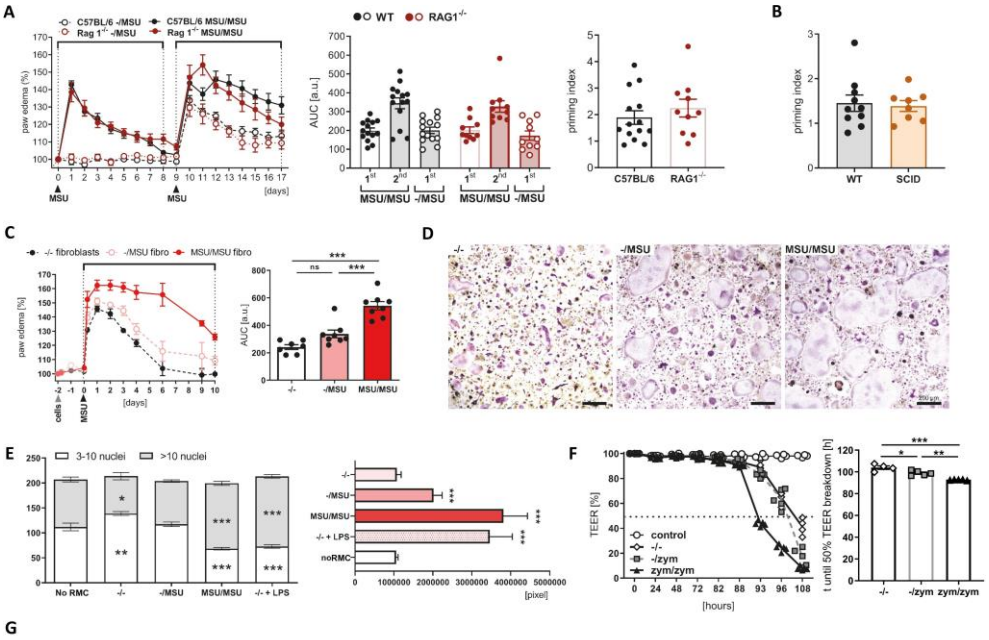

G

Macrophage data

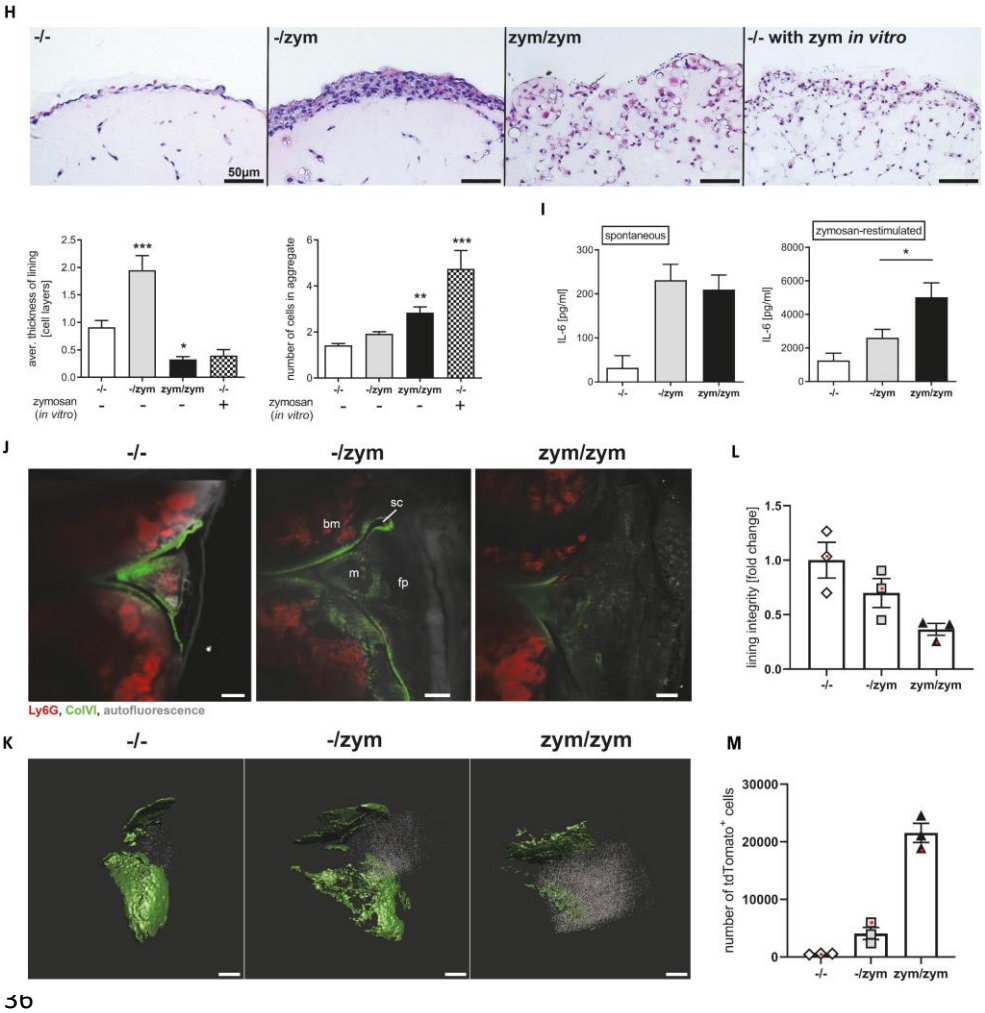

Figure 2. Functional changes of articular fibroblasts mediate prolonged arthritis and bone remodeling. (A, B) Development of inflammatory tissue priming is not inhibited in the absence of functional T and B cells in RAG1^{ko} mice **(A)** and SCID mice **(B). (A)** Disease course (left panel), area under the curves (AUC, middle) and priming indices (right) during iterated MSU crystal-induced arthritis in RAG^{ko} (N = 10) and C57BL/6 wildtype (WT) mice (N = 14). Priming index is defined as the ratio between AUC of the second episode of arthritis and the first episode of arthritis in the contralateral paw. **(B)** Priming indices of iterated zymosan-induced arthritis in SCID mice (N = 8) and BALB/c WT mice (N = 10). **(C)** Injection of primed fibroblasts (MSU/MSU) sensitizes joints for prolonged arthritis. Disease course of MSU crystal-induced arthritis induced 2 days after injection of cultured fibroblasts derived from naïve, non-primed (-/MSU) or primed (MSU/MSU) paws. Shown are disease curves and AUC (N = 7-8). **p < 0.01, ***p < 0.001, as determined by ANOVA with Tukey´s multiple comparisons test. **(D, E)** Osteoclast differentiation from bone marrow cells in co-culture with non-primed, primed or naive fibroblasts (with or without stimulation with LPS). Shown are representative TRAP-stained images **(D)**, number of small (3-10 nuclei) and large (>10 nuclei) osteoclasts (**E**, left panel), and means and SEM of total area covered by osteoclasts (**E**, right panel). *p < 0.05, **p < 0.01, ***p < 0.001, as determined by ANOVA with Dunnett´s multiple comparisons test. N = 5-7. **(F)** Matrix-invasive capacity of naïve (-/), non-primed (-/zym) and primed (zym/zym) fibroblasts (N = 4-5), demonstrated by the percent decrease in the transepithelial electrical resistance (TEER). The MDCK-C7 layer alone served as internal assay control. Dashed line indicates 50% breakdown of TEER. *p < 0.05, **p < 0.01, ***p < 0.001, ANOVA with Tukey´s test. **(G)** Development of iterated MSU crystal-induced arthritis in pre-depleted Cx3cr1cre:iDTR mice (n = 6) and iDTR control mice (n= 9) treated with diphtheria toxin (DT) 5 and 6 days before the second injection of MSU crystals. Shown are disease course (left panel) and priming indices (right panel). **(H)** Assessment of lining formation and interconnectivity in 3D organ cultures from naïve (-/-), non-primed (-/zym) and primed (zym/zym) rat fibroblasts with our without zymosan restimulation *in vitro*. Shown are representative images of H&E stained sections from 3D organ cultures and quantification of lining layer thickness and cell connections in the sublining. Bar diagrams show means and S.E.M. (N = 3-5). *p < 0.05, **p < 0.01, ***p < 0.001, ANOVA with Dunnet´s test. **(I)** Interleukin (IL)-6 concentrations in supernatants from 3D organ cultures with or without *in vitro* stimulation with zymosan. *p < 0.05, paired t-test. **(J)** Representative 3D light-sheet fluorescence microscopy (LSFM) of knee joints of *ColVI^{cre}:R26-tdTomato* mice injected once or twice with zymosan or left uninjected. Arrowheads indicate the localization of the fibroblast layer (green) at the border of the synovial cavity. bm, bone marrow; fp, infrapatellar fat pad; m, meniscus; sc, synovial cavity. Scale bars, 200 µm. **(K)** Representative LSFM-derived 3D reconstruction of tdTomato^{+} cells in the synovial membrane (green) and the synovial sublining tissue (grey) from the knees of *ColVI^{cre}:R26-tdTomato* mice. Scale bars, 300 µm. (**L**) Quantification of lining integrity in the synovial membrane, normalized to mean values from -/- paws. **(M)** Quantification of tdTomato^{+} cells in the sublining synovial tissue of mouse knees during iterated zymosan-induced arthritis. Data are shown as individual values, mean ± S.E.M. N = 3. Samples shown in (J, K) are indicated with a red dot.

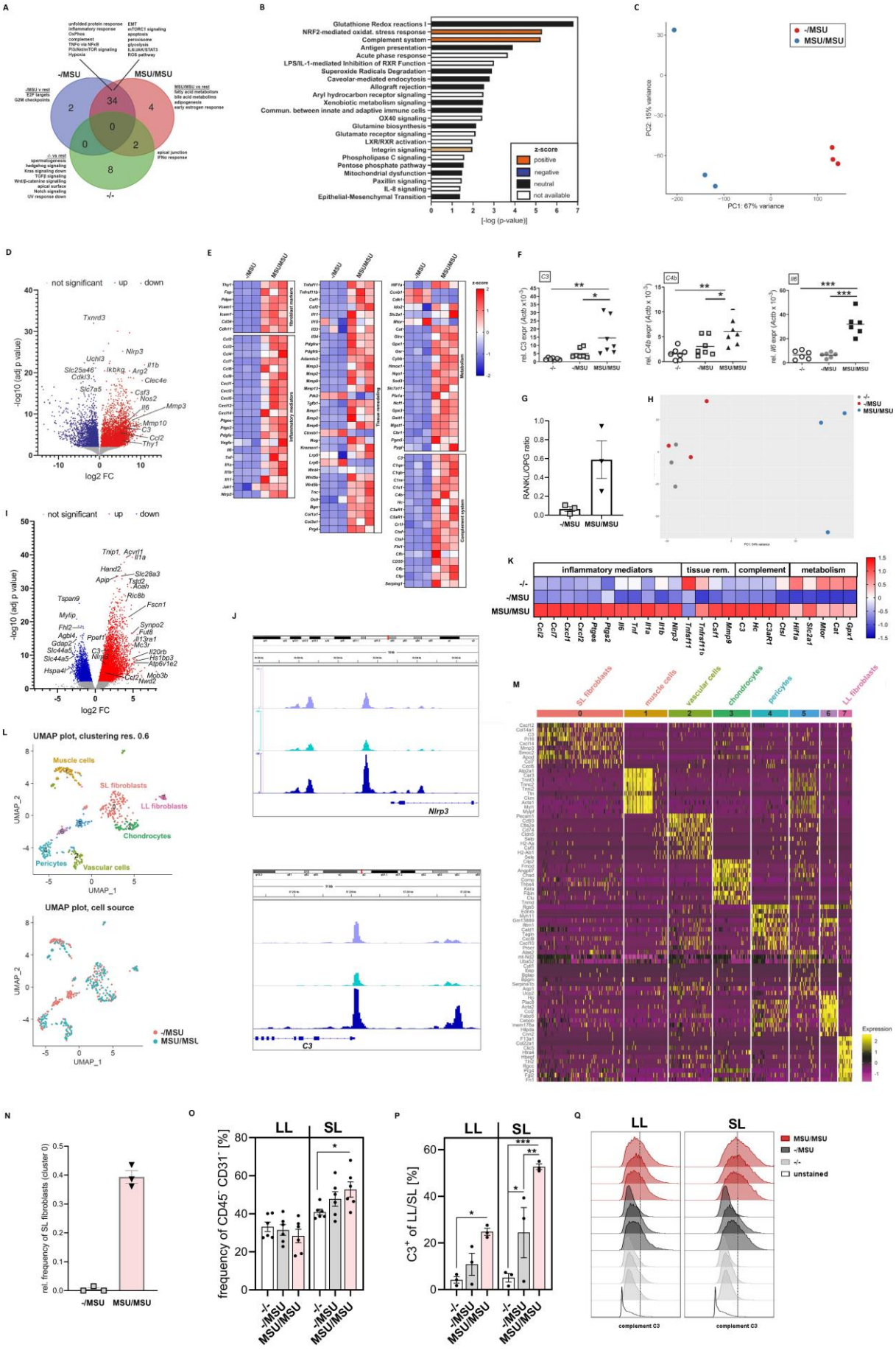
A
-/MSU
MSU/MSU
-/-
B
Glutathione Redox reactions I
NRF2-mediated oxidat. stress response
Complement system
Antigen presentation
Acute phase response
LPS/IL-1-mediated Inhibition of RXR Function
Superoxide Radicals Degradation
Caveolar-mediated endocytosis
Allograft rejection
Aryl hydrocarbon receptor signaling
Xenobiotic metabolism signaling
Commun. between innate and adaptive immune cells
OX40 signaling
Glutamine biosynthesis
Glutamate receptor signaling
LXR/RXR activation
Integrin signaling
Phospholipase C signaling
Pentose phosphate pathway
Mitochondrial dysfunction
Paxillin signaling
IL-8 signaling
Epithelial-Mesenchymal Transition
z-score
positive
negative
neutral
not available
[-log (p-value)]
C
-/MSU
MSU/MSU
PC2: 15% variance
PC1: 67% variance
D
not significant
up
down
-log10 (adj p value)
log2 FC
E
-/MSU
MSU/MSU
Fibroblast markers
Inflammatory mediators
Tissue remodeling
Metabolism
Complement system
z-score
F
C3
C4b
Il6
rel. C3 expr (Actb x 10-3)
rel. C4b expr (Actb x 10-3)
rel. Il6 expr (Actb x 10-3)
-/-
-/MSU
MSU/MSU
G
RANKL/OPG ratio
H
-/-
-/MSU
MSU/MSU
I
not significant
up
down
-log10 (adj p value)
log2 FC
J
Nlrp3
C3
K
inflammatory mediators
tissue rem.
complement
metabolism
-/-
-/MSU
MSU/MSU
Ccl2
Ccl7
Cxcl1
Cxcl2
Ptgs2
Il6
Tnf
Il1a
Il1b
Nlrp3
Tnfsrf11
Tnfsrf11b
Csf1
Mmp9
C3
Hc
C3aR1
Ctsl
Hif1a
Slc2a1
Mtor
Cat
Gpx1
L
UMAP plot, clustering res. 0.6
Muscle cells
SL fibroblasts
LL fibroblasts
Chondrocytes
Pericytes
Vascular cells
UMAP_1
UMAP_2
UMAP plot, cell source
-/MSU
MSU/MSU
M
SL fibroblasts
muscle cells
vascular cells
chondrocytes
pericytes
LL fibroblasts
Expression
N
rel. frequency of SL fibroblasts (cluster 0)
-/MSU
MSU/MSU
O
LL
SL
frequency of CD45- CD31- [%]
-/-
-/MSU
MSU/MSU
P
LL
SL
C3+ of LL/SL [%]
-/-
-/MSU
MSU/MSU
Q
LL
SL
MSU/MSU
-/MSU
-/-
unstained
complement C3
complement C3

Figure 3. Transcriptomic profiling of articular fibroblasts from iterated MSU crystal-induced arthritis. Fibroblasts from paws of naïve mice (-/-, n=3), and from paws injected with MSU crystals once (non-primed, -/MSU; n=3) or twice (primed, MSU/MSU; n=3) were cultivated and transcriptomic analyses performed after bulk RNA sequencing using an rRNA depletion method. **(A)** Venn diagram of differentially regulated pathways of gene set enrichment analysis (GSEA). **(B)** Ingenuity pathway analysis showing canonical pathways differentially regulated in primed fibroblasts as compared to non-primed fibroblasts. **(C)** Principal component analysis (PCA) of cultured non-primed (-/MSU) and primed (MSU/MSU) fibroblasts after bulk RNA sequencing using mRNA enrichment. **(D)** Volcano plot of differential gene expression in MSU/MSU as compared to -/MSU fibroblasts (n = 3). **(E)** Expression Z-scores of selected genes generated from bulk RNA sequencing. Data are from non-primed and primed fibroblasts (n = 3). **(F)** Confirmatory quantitative RT–PCR analysis in *in vitro* cultured naive, non-primed and primed fibroblast subsets determining expression of mRNAs encoding C3 (n = 7), C4b (n = 7) and IL-6 (n = 6). Shown are individual values and means. *p < 0.05, **p < 0.01, ***p < 0.001, ANOVA with Tukey´s multiple comparisons test. **(G)** RANKL/OPG ratios in non-primed and primed fibroblasts calculated from RPKM values of bulk RNA Sequencing. **(H)** Principal component analysis of naive (-/-), non-primed (-/MSU) and primed (MSU/MSU) synovial fibroblasts based on ATAC-seq peak location and intensity. **(I)** Volcano plot of gene-annotated open chromatin regions in MSU/MSU as compared to -/MSU fibroblasts (n = 2-3). **(J)** Representative Integrative Genomics Viewer Browser tracks displaying normalized profiles for ATAC-Seq signals around the transcription start sites (TSS) of the *C3* and the *Nlrp3* gene. Each lane shows pooled data from 3 replicates of fibroblasts. **(K)** Mean Z-scores of selected genes generated from ATAC Seq counts (n = 3 replicates per condition). Quantification involved 3 kbp regions around the TSS. (**L, M)** Differential gene expression between clusters from single-cell RNA sequencing of $CD45^-$ cells from non-primed and primed paws. The UMAP plots **(L)** depict the initial automatic cluster assignments from Seurat. The lower panel shows the same UMAP plot coloured by origin from non-primed and primed paws. The heat map **(M)** shows the (row-scaled) expression of the top-10 (by fold change) significant marker genes for each cluster (FDR, Benjamini–Hochberg adjusted) in the downsampled integrated dataset comprising the non-primed (-/MSU) and the primed (MSU/MSU) data. Each column represents a single cell and each row shows the given gene. SL, sublining layer fibroblasts; LL, lining layer fibroblasts. **(N)** Relative frequencies of sublining (SL) fibroblasts in primed and non-primed fibroblast populations, deconvoluted from bulk RNA sequencing data using single-cell RNA sequencing reference profiles. **(O - Q)** Flow cytometric characterization of synovial fibroblast marker expression in naïve paws and in paws two days after the first (-/MSU, non-primed paw) and second (MSU/MSU, primed paw) injection of MSU crystals. Shown are individual values and means of percentages of **(O)** LL ($CD45^-CD31^-Pdpn^+Thy1^+$) and SL ($CD45^-CD31^-Pdpn^+Thy1^+$) fibroblasts (n = 6) and **(P)** of complement C3-positive cells in LL and SL fibroblasts (n = 3). Plots show individual values and means, every symbol represents pooled cells from two mice. **(Q)** Overlay of mean fluorescence intensities of complement C3 in SL and LL fibroblasts of naive, non-primed and primed paws. Dashed lines indicate cutoff values for $C3^+$ cells depicted in **(P)**.

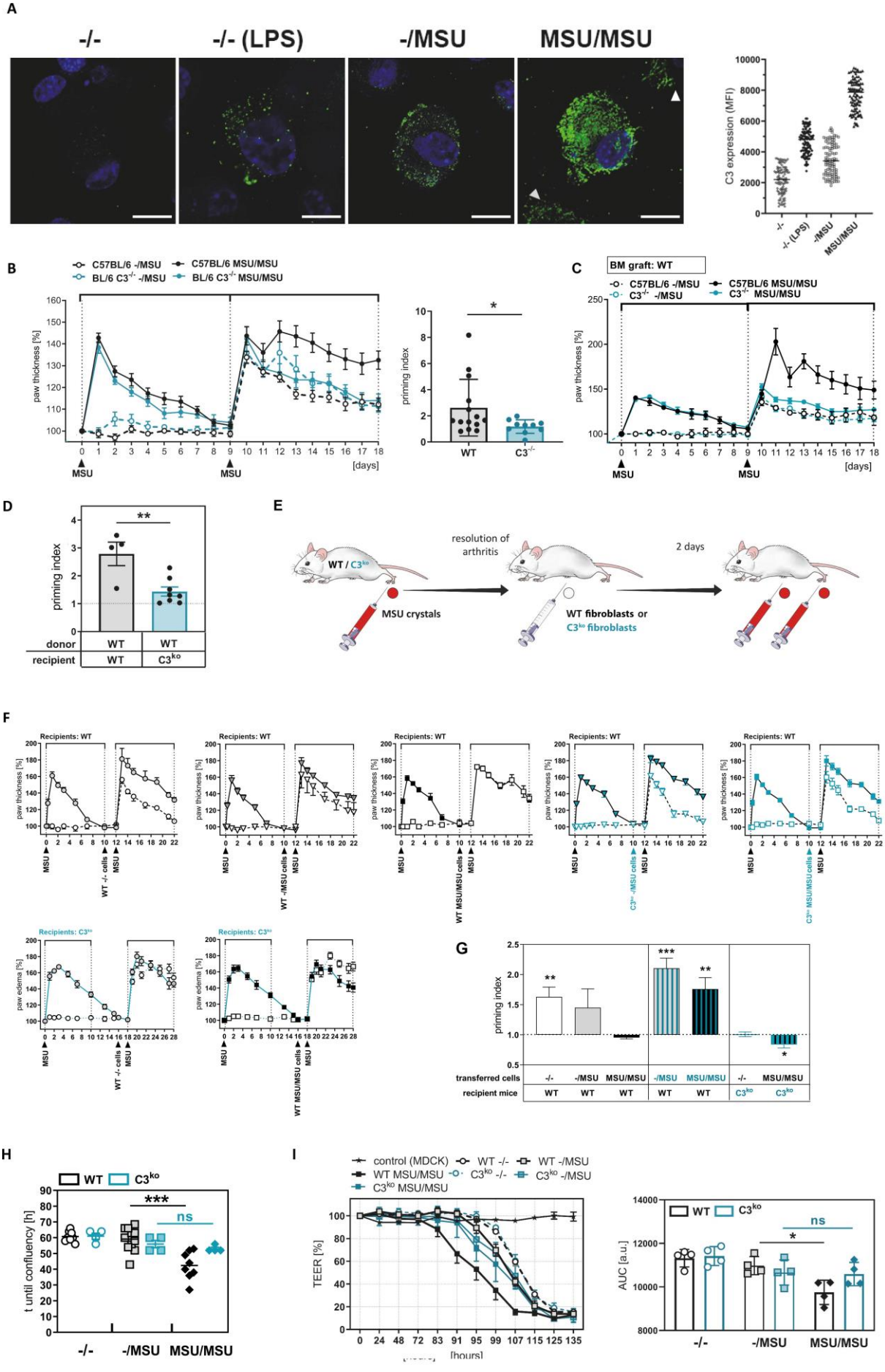
A
-/-
-/- (LPS)
-/MSU
MSU/MSU
C3 expression (MFI)
B
C57BL/6 -/MSU
C57BL/6 MSU/MSU
BL/6 C3-/- -/MSU
BL/6 C3-/- MSU/MSU
paw thickness [%]
priming index
WT
C3-/-
MSU
[days]
C
BM graft: WT
C57BL/6 -/MSU
C3-/- -/MSU
C57BL/6 MSU/MSU
C3-/- MSU/MSU
D
priming index
donor
recipient
WT
C3ko
E
WT / C3ko
MSU crystals
resolution of arthritis
WT fibroblasts or C3ko fibroblasts
2 days
F
Recipients: WT
Recipients: C3ko
paw thickness [%]
paw edema [%]
WT -/- cells
WT -/MSU cells
WT MSU/MSU cells
C3ko -/MSU cells
C3ko MSU/MSU cells
G
priming index
transferred cells
recipient mice
H
t until confluency [h]
ns
I
control (MDCK)
WT -/-
WT -/MSU
WT MSU/MSU
C3ko -/-
C3ko -/MSU
C3ko MSU/MSU
TEER [%]
[hours]
AUC [a.u.]

Figure 4. Complement component 3 (C3) upregulation in articular fibroblasts mediates pathogenic function and inflammatory tissue priming. (A) Representative confocal microscopy images and quantification of intracellular expression of C3 in 100 fibroblasts per condition. Arrowheads indicate extracellular C3 apposition. Scale bars, 5 µm. **(B)** Course of paw swelling and priming indices of iterated monosodium urate (MSU) crystal-induced arthritis in C57BL/6 wildtype (WT) and C3-deficient ($C3^{ko}$) mice (n = 10-13). *p < 0.05, as determined by Mann-Whitney U-test. **(C, D)** Course of paw swelling **(C)** and priming indices **(D)** of iterated MSU crystal-induced arthritis in irradiated WT and $C3^{ko}$ mice after stable reconstitution with WT bone marrow. N = 4-8. **(E-G)** Induction of inflammatory tissue priming by injection of sorted cultured $CD45^{-}CD31^{-}$ naive (-/-), non-primed (-/MSU), or primed (MSU/MSU) fibroblasts from WT or $C3^{ko}$ mice into previously uninjected WT and $C3^{ko}$ paws. N = 3-8. **(E)** Injection scheme of inflammatory tissue priming by transfer of fibroblasts. Course of arthritis **(F)** and priming indices **(G)** after transfer of primed WT or C3-deficient fibroblasts into the paws of WT or $C3^{ko}$ mice. * p < 0.05, ** p < 0.01, *** p < 0.001, as determined by One sample t-test. **(H)** Quantitative assessment of a wound healing/migration assay with fibroblasts isolated from naïve or MSU crystal-injected paws from C57BL/6 WT or C3-deficient mice. N = 4-12. ***p < 0.001, n.s., not significant, ANOVA with Tukey´s multiple comparisons test. **(I)** Matrix invasion of WT and C3-deficient fibroblasts isolated from naïve and MSU-injected paws, shown as the decrease of transepithelial electrical resistance (TEER) indicating disturbance of an MDCK epithelial cell layer (N = 4).

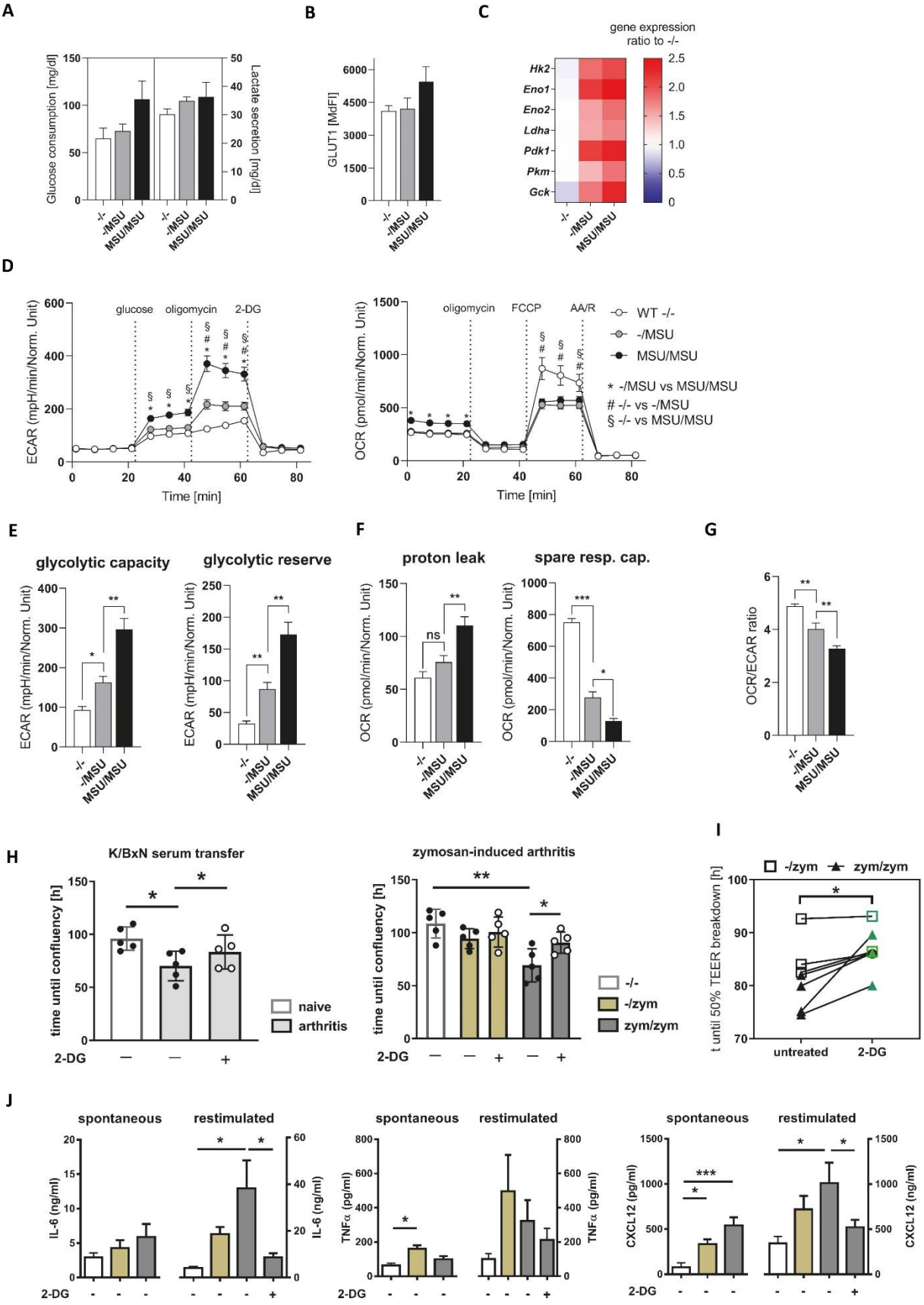

Figure 5. Metabolic shift during establishment of inflammatory tissue priming in arthritis. (A) Glucose consumption and lactate secretion were analyzed in culture supernatants from naïve (-/-, n=5), non-primed (-/MSU, n=7), and primed (MSU/MSU, n = 9) articular fibroblasts. **(B)** Surface expression of the

glucose transporter GLUT1 was assessed from the same fibroblast samples (n = 7-9) by means of flow cytometry. **(C)** Gene expression of key glycolytic enzymes was determined by RNA sequencing and calculated as the ratio to the mean normalized counts of the -/- derived fibroblast values (n=3). **(D)** Bioenergetics of -/- (n=3), -/MSU (n=7), and MSU/MS-derived (n=7) fibroblasts were recorded with a Seahorse XFe96 device and normalized to background and total protein. *p < 0.01 of -/MSU vs MSU/MSU, # p < 0.01 of -/- vs -/MSU, § p < 0.01 of -/- vs MSU/MSU. From these data key glycolytic **(E)** and respiratory **(F)** parameters as well as the ratio **(G)** between OCR (as surrogate for mitochondrial respiration) and ECAR (as surrogate for aerobic glycolysis) were calculated. *p < 0.05, **p < 0.01, ***p < 0.001, as determined by Kruskal-Wallis test. Ns, not significant. **(H)** Quantitative assessment of a wound healing/migration assay showing fibroblasts isolated from naïve or arthritic mouse paws. Treatment with 2 mM 2-deoxy-D-glucose (2-DG) reconstituted enhanced wound healing/migration seen in fibroblasts isolated from K/BxN serum transfer arthritis (left panel, n = 5) or zymosan-induced arthritis (right panel, n = 5) to levels measured in naïve fibroblasts. *p < 0.05, **p < 0.01, as determined by paired t-test. **(I)** Decline of invasiveness of fibroblasts isolated from paws injected with zymosan once (n = 3) or twice (n = 4) upon treatment with 2-DG. *p < 0.05, paired t-test. **(J)** Concentrations of IL-6, TNFα, and CXCL12 in supernatants of unstimulated mouse fibroblasts (spontaneous) and fibroblasts re-stimulated *in vitro* with zymosan and incubated with or without 2-DG (n=5). *p < 0.05, ***p < 0.001, ANOVA with Tukeys´ multiple comparisons test.

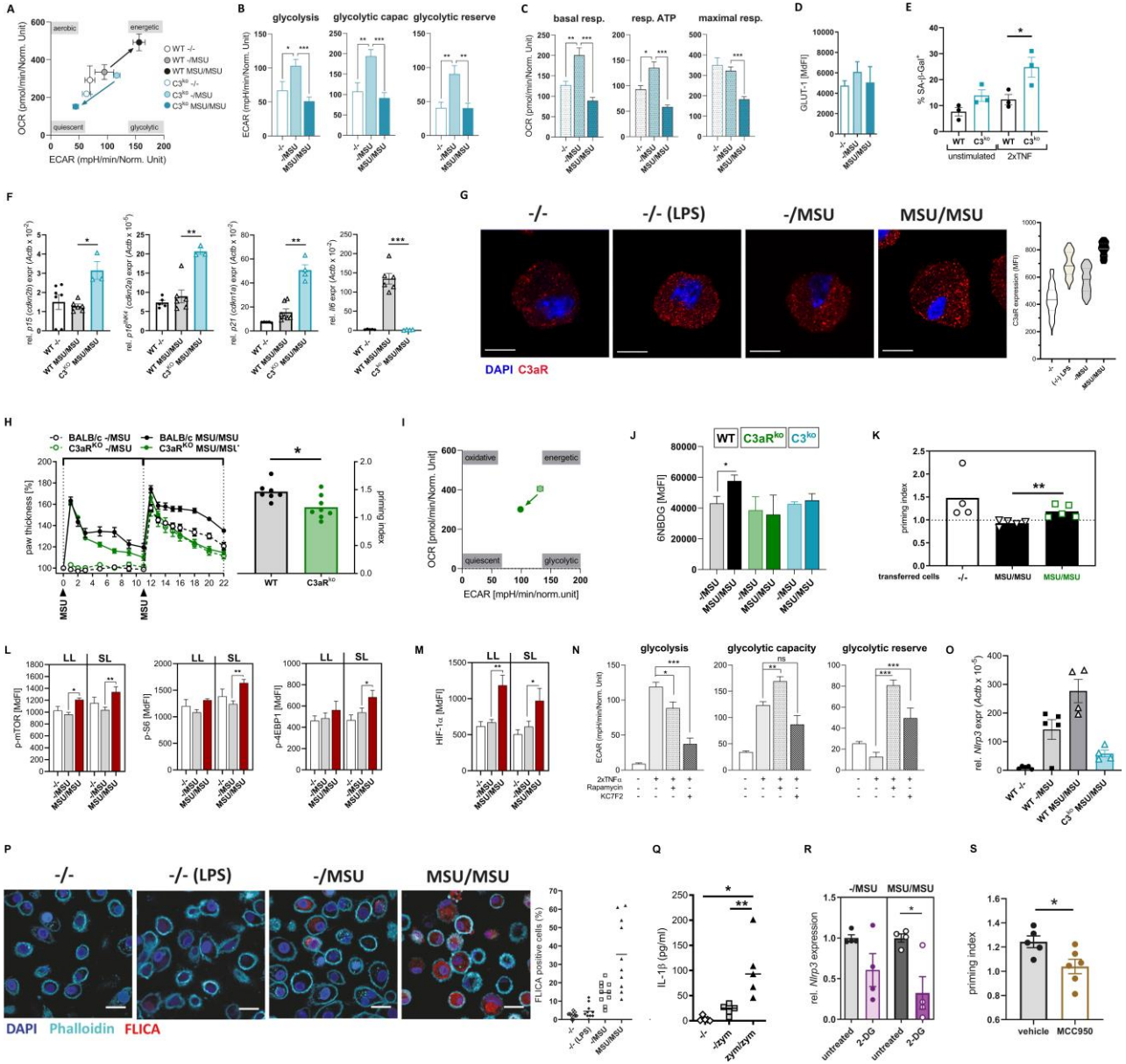
A
aerobic
energetic
quiescent
glycolytic
OCR (pmol/min/Norm. Unit)
ECAR (mpH/min/Norm. Unit)
WT -/-
WT -/MSU
WT MSU/MSU
C3ko -/-
C3ko -/MSU
C3ko MSU/MSU
B
glycolysis
glycolytic capac
glycolytic reserve
C
basal resp.
resp. ATP
maximal resp.
D
GLUT-1 [MdFI]
E
% SA-β-Gal+
unstimulated
2xTNF
F
G
-/-
-/- (LPS)
-/MSU
MSU/MSU
DAPI C3aR
H
BALB/c -/MSU
C3aRKO -/MSU
BALB/c MSU/MSU
C3aRKO MSU/MSU
paw thickness [%]
priming index
MSU
I
oxidative
energetic
quiescent
glycolytic
J
WT
C3aRko
C3ko
6NBDG [MdFI]
K
priming index
transferred cells
L
LL
SL
p-mTOR [MdFI]
p-S6 [MdFI]
p-4EBP1 [MdFI]
M
HIF-1α [MdFI]
N
glycolysis
glycolytic capacity
glycolytic reserve
ECAR (mpH/min/Norm. Unit)
2xTNFα
Rapamycin
KC7F2
O
rel. Nlrp3 expr (Actb x 10-5)
P
-/-
-/- (LPS)
-/MSU
MSU/MSU
DAPI Phalloidin FLICA
FLICA positive cells (%)
Q
IL-1β (pg/ml)
-/-
-/-zym
-/-zym/zym
R
-/MSU
MSU/MSU
rel. Nlrp3 expression
untreated
2-DG
S
priming index
vehicle
MCC950

Figure 6. Complement C3 mediates metabolic changes that mediate inflammatory memory. (A) Energy map of naïve (-/-), non-primed (-/MSU) and primed (MSU/MSU) articular fibroblasts from wild type (WT) and C3-deficient ($C3^{ko}$) mice as assessed by metabolic flux analysis of ECAR and OCR normalized to background and total protein. **(B, C)** Key glycolytic (B) and respiratory (C) parameters calculated from normalized (background and protein) metabolic flux data of -/-, -/MSU or MSU/MSU fibroblasts from $C3^{ko}$ mice. *p < 0.05, **p < 0.01, ***p < 0.001, paired t-test. **(D)** Surface expression of the glucose transporter GLUT1 in fibroblast samples from $C3^{ko}$ mice (n = 2-4). **(E)** Percentages of senescence-activated beta galactosidase (SA-β-Gal)-positive fibroblasts (blue staining) derived from passage 8 and repeatedly incubated with or without TNFα. **(F)** Quantitative RT-PCR analysis in *in vitro* cultured WT and $C3^{ko}$ fibroblasts determining expression of the senescence markers *p15*, *16^{INK4}*, and *p21*, and of *Il6.* * p < 0.05, ** p < 0.01, Student´s t-test. N = 3-7. **(G)** Representative confocal microscopy images and quantification of C3a receptor (C3aR) expression in fibroblasts. Shown is staining of nuclei (DAPI, blue) and C3aR (red). Scale bars, 10 µm. Violin plots show median and quartiles of 100 cells. **(H)** Course of paw swelling and priming indices of iterated MSU crystal-induced arthritis in BALB/c WT and C3aR-deficient ($C3aR^{ko}$) mice (n = 7-8). * p < 0.05, as determined by Student´s t-test. **(I)** Energy map of non-primed (-/MSU) and primed (MSU/MSU) articular fibroblasts from $C3aR^{ko}$ mice as assessed by metabolic flux analysis of ECAR and OCR normalized to background and total protein. **(J)** Median fluorescence intensity (MdFI) of the fluorescent nonhydrolyzable glucose analog 6NDGB in non-primed and primed fibroblasts from WT (BALB/c), $C3^{ko}$ and $C3aR^{ko}$ mice. * p < 0.05, as determined by ... N = ? **(K)** Priming indices after transfer of naïve (-/-) or primed (MSU/MSU) WT (BALB/c) or C3aR-deficient fibroblasts into the paws of WT BALB/c mice. ** p < 0.01, as determined by Student´s t-test. N = 4-5. **(L)** Flow cytometric analysis of mTOR, 4-EBP1 and S6 phosphorylation in $CD45^{-}CD31^{-}Pdpn^{+}Thy1^{-}$ lining layer (LL) and $CDC45^{-}CD31^{-}Pdpn^{+}Thy1^{+}$ sublining (SL) fibroblasts from collagenase-digested naïve (-/-) paws and from paws 2 days after the first (-/MSU) or second (MSU/MSU) injection of MSU crystals. N = 3 (p-mTOR and p-S6) or 6 (p-4EBP1).* p < 0.05, ** p < 0.01, Student´s t-test. **(M)** HIF-1α expression in LL and SL fibroblasts from collagenase-digested naïve paws and from paws 2 days after the first or second injection of MSU crystals, as determined by flow cytometry. * p < 0.05, ** p < 0.01, Students t-test. N = 4. **(N)** Key glycolytic parameters in naïve WT synovial fibroblasts (n = 2 replicates of pooled cells from two mice) after two stimulation rounds with 10 ng/ml TNFα in the presence or absence of rapamycin (50 µM) or KC7F2 (30 µM), as recorded by Seahorse and normalized to background and total protein. *** p < 0.001. **(O)** Quantitative RT–PCR analysis in *in vitro* cultured WT (C57BL/6) and $C3^{ko}$ fibroblasts determining expression of mRNA encoding *Nlrp3* (n = 4-6). Shown are individual values and means. **(P)** Representative confocal microscopy images and quantification of caspase-1 enzymatic activity in fibroblasts by labelling with FAM-YVAD-FMK (FLICA). Shown is staining of nuclei (DAPI, blue), F-actin (phalloidin, turquoise) and FLICA (red). Scale bars, 20 µm. **(Q)** Concentration of IL-1β in supernatants of naïve (-/-), non-primed (-/MSU) and primed (MSU/MSU) fibroblasts. Graph shows individual values and means, n=5. *p < 0.05, **p < 0.01, ANOVA with Tukeys´ multiple comparisons test. **(R)** Drop in expression of *Nlrp3* in non-primed (-/MSU) and primed (MSU/MSU) fibroblasts cultured for 24h with 2-mM 2-DG, as determined by qPCR. N = 4**.** *p < 0.05, ANOVA with Tukey´s multiple comparison test. **(S)** Priming indices of iterated MSU crystal-induced arthritis upon treatment with the NLRP3 inflammasome inhibitor MCC950 or vehicle. MCC950 abrogates development of inflammatory tissue priming. Scale bars, 1 mm. *p < 0.05, as determined by Student´s t-test.

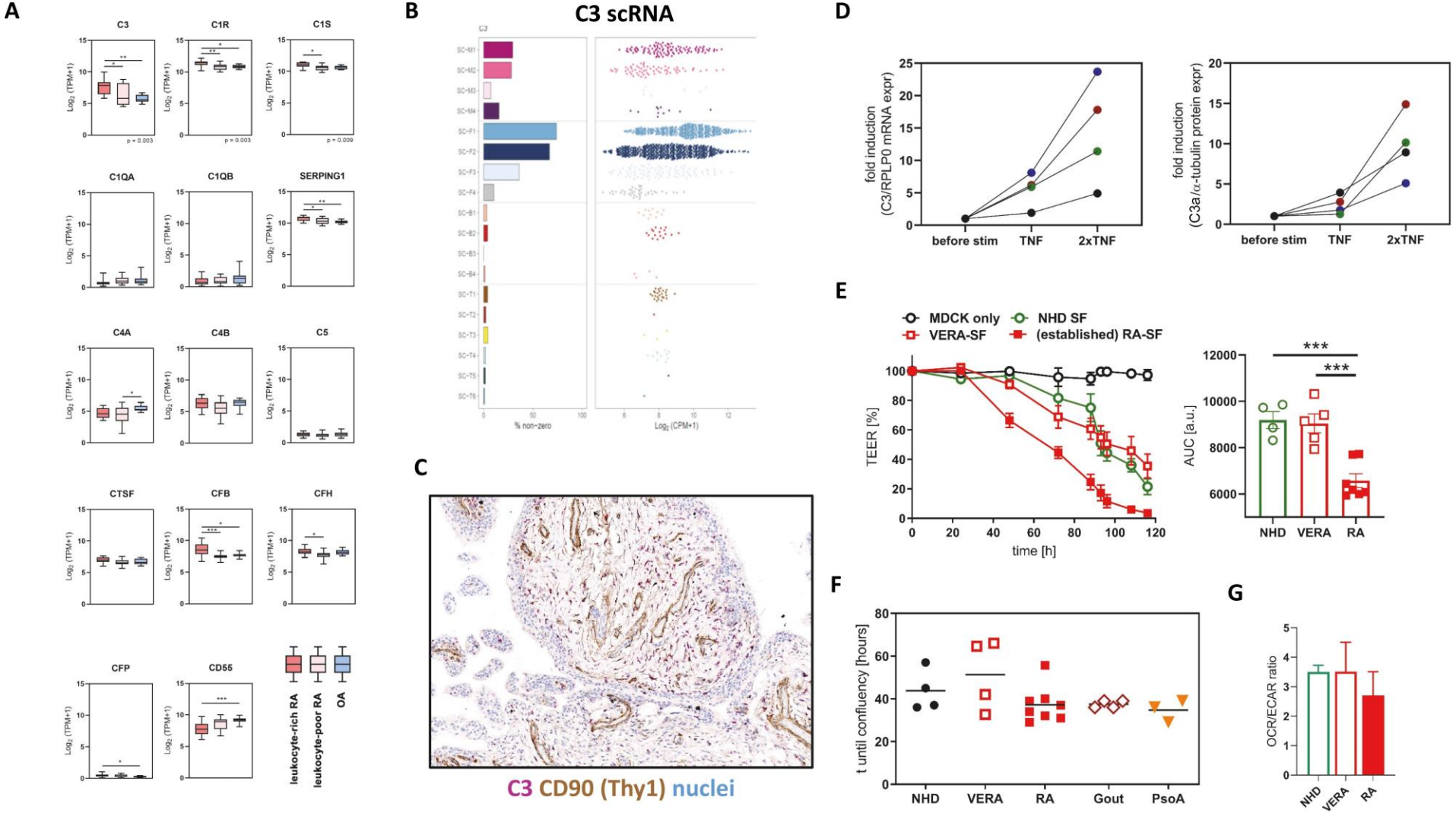
A
C3
C1R
C1S
C1QA
C1QB
SERPING1
C4A
C4B
C5
CTSF
CFB
CFH
CFP
CD55
leukocyte-rich RA
leukocyte-poor RA
OA
B
C3 scRNA
% non-zero
C
C3 CD90 (Thy1) nuclei
D
fold induction (C3/RPLP0 mRNA expr)
fold induction (C3a/α-tubulin protein expr)
before stim
TNF
2xTNF
E
MDCK only
VERA-SF
NHD SF
(established) RA-SF
TEER [%]
time [h]
AUC [a.u.]
NHD
VERA
RA
F
t until confluency [hours]
NHD
VERA
RA
Gout
PsoA
G
OCR/ECAR ratio
NHD
VERA
RA

Figure 7. The complement system is upregulated in activated sublining synovial fibroblast of human individuals with inflammatory arthritis. (A) Expression values (shown as transcripts per kilobase million +1) from various complement proteins derived from bulk RNA sequencing on $CD45^{-}Pdpn^{+}$ fibroblasts from synovial tissue of individuals with leukocyte-rich rheumatoid arthritis (RA, n = 16), leukocyte-poor RA (n = 17) and osteoarthritis (OA, n= 12). Shown are medians, 25^{th} and 75^{th} percentile (boxes), range (whiskers), and individual values. *p < 0.05, **p < 0.01, ***p < 0.001, as calculated by Kruskal-Wallis test with Dunn´s multiple comparisons test. **(B)** Single cell RNASeq of human synovial membrane showing expression of complement component C3 in fibroblast and leukocyte subsets. **(C)** RNAScope *in situ* hybridization of an OA-derived synovium showing accumulation of C3 expressing cells in the sublining**. (D)** C3 mRNA expression related to expression of RPLP0 (left panel) and quantification of C3 alpha chain derived from Western blot (right panel) in cultured fibroblasts from 4 individuals with RA and after repeated stimulation with TNF *in vitro*. Data are normalized to expression values before stimulation. **(E)** Decrease of transepithelial electrical resistance (TEER) in a MATRIN assay using fibroblasts isolated from individuals with very early RA (VERA, n = 5), established RA (n = 8) and normal healthy donors (NHD, n = 4). **(F)** Quantitative assessment of a wound healing/migration assay, shown as hours until confluency, with fibroblasts isolated from NHD (n = 4), VERA (n = 4), established RA (n = 7), gouty arthritis (n = 4) and psoriatic arthritis (PsoA, n = 3). **(G)** Glycolytic shift of synovial fibroblasts from RA patients (n=3) compared to fibroblasts from NHDs (n=2) or VERA (n=3) as assessed by OCR/ECAR ratio.